Monte Carlo simulations and measurements of the radiation environment at a laser-plasma accelerator

Jack Strand Berg

Supervisors:
Martin Hansson, Olle Lundh

October 14, 2016

Abstract

In current experiments at the high-power laser facility at the Lund Laser Centre, electrons accelerated to hundreds of MeV over short distances by means of laser wakefield acceleration in produced plasmas.

To determine the amount of secondary radiation generated when accelerated electrons interact with surrounding materials is of interest to ensure a safe working environment. In this thesis, the radiation levels inside the laboratory are simulated using GEANT4, a C++ class library for particle physics and particle tracking using Monte Carlo methods.

For persons directly outside the room of the vacuum chamber, conservative simulation results indicate that even for electrons accelerated to a relatively large average energy of 500 MeV, in bunches containing an average charge of 100 pC, in excess of 10^8 shots would need to be fired in a single year to reach doses of the order of the limits set by the Swedish Radiation Safety Authority. At a pulse rate of 0.1 shots per second, this corresponds to continuous operation for 27 700 hours.

As a test of the simulations, experimental dose data were collected using dosimetric instruments – measuring doses from electron, gamma and neutron radiation – showing agreement with simulated doses to within reasonable error .

Contents

Popular science summary

At the Lund High Power Laser facility, electrons are accelerated to energies of several hundred MeV in just a few millimeters—reaching velocities of 99.9999 % of the speed of light. When these electrons hit the surrounding walls and equipment in the laboratory, secondary radiation is generated as other particles are knocked out in electromagnetic and nuclear interactions. In this thesis, this secondary radiation is simulated to make sure that persons working in the laboratory are not subjected to harmful radiation levels.

Acceleration of electrons is achieved by sending short laser pulses of high power onto a gaseous target. The power in a single laser pulse reaches the order of tens of terawatt, equivalent to the power output of thousands of nuclear power plants. As the laser pulse hits the gas, the optical fields are strong enough to pull the electrons from the nucleus, separating negative and positive charges from each other, thus ionizing the gas. The ionization occurs for many atoms at the same time which means that part of the gas is turned into a plasma. Now it no longer behaves like a gas of individual molecules. Instead, the plasma has a more complex collective behavior similar to that of a fluid, but strongly driven by electromagnetic interactions. As the laser pulse travels through the plasma, electrons are subjected to a strong force which pushes them away, both forwards and radially outwards. This force is strong enough to create a bubble following the laser pulse which is completely empty of electrons and therefore carries a large positive charge. If a small fraction of electrons are placed inside this bubble, they will be strongly attracted by the positive charge of the bubble and become trapped inside it. Trapped electrons are now quickly accelerated to high energies when the bubble follows the laser pulse.

Simulations of the radiation environment start with the accelerated electron beam and does not include the laser-plasma interactions themselves. The accelerated electrons originate from the center of a vacuum chamber made out of aluminum. When an accelerated electron enters the aluminum, a large number of processes can occur, producing secondary particles which in turn may undergo secondary processes, producing even more particles. The accelerated electrons and any secondary particles that manage to pass through the aluminum will then undergo similar processes as they hit the concrete walls in the laboratory. All particles generated in these processes,

as well as the primary accelerated electrons, are tracked until they have lost all their energy and stop. To simulate these particle interactions and the production of secondary particles, so called, *Monte Carlo methods* are used, where a large number of primary electrons and secondary particles (e.g. photons and neutrons) are traced using statistical methods. This means that for each step in the simulation all the possible events are given a certain weight according to their relative probabilities of occurring. These probabilities are either determined from theoretical models or from experimental data. To pick one event from the complete probability distribution of all possible events, a random number generator is used.

Results from the simulations indicate that using the current experimental setup, the radiation levels during one year are more than 20,000 times below the safe limit when the correct safety precautions are taken. They also indicate that the experiments are not without danger as a person standing directly in the electron beam would reach the yearly radiation limit within less than an hour of operation.

Chapter 1

Introduction

This thesis treats the radiation environment of the laser-plasma experiments at the multi-terawatt laser at the High Power Laser Facility at the Lund Laser Centre—as a part of measures taken to ensure that the researchers connected to those experiments are subjected radiation levels within safe limits. Here, work is currently being done on acceleration of electrons, protons and positive ions by focusing short laser pulses onto solid or gaseous targets. The power of each laser pulse used reaches 20 TW, with peak intensities in the focus of $10^{18} - 5 \times 10^{19}$ W/cm^2. The target is typically a gas jet in experiments on electron acceleration and a thin metallic foil in experiments on proton acceleration. The laser pulse itself typically has a duration of less than 40 fs. In the interaction between the laser pulses and gaseous target, electrons can be accelerated up to relativistic energies typically less than 300 MeV but always less than 500 MeV in bunches of total charge up to hundreds of pC.

The high particle energy content gives rise to the generation of secondary radiation due to interactions with the surrounding materials. This secondary radiation primarily consists of electrons and photons originating from bremsstrahlung cascades and neutrons produced in photo-nuclear interactions when a bremsstrahlung photon interacts with the protons and neutrons of a nucleus. The aim of this thesis is to characterize this secondary radiation and produce an estimate of the radiation dose levels that persons inside the laboratory are subjected to during operation, to confirm that this is a safe work environment.

Simulations on radiation doses are performed using GEANT4 [1, 2], a C++ class library for particle tracking using Monte Carlo methods. GEANT4 lets one specify a geometry and its material composition together with a primary particle source. Each primary particle (and its daughters) is then tracked throughout the geometry. These simulations do not include the laser-plasma interactions themselves but are based on properties of the accelerated electron and proton beams. Water phantoms are used as human tissue equivalents and the energy deposited are collected to determine doses at different locations inside the laboratory. Maps over dose distributions are

produced by scoring particle fluxes which is then converted to dose.

As a test of the simulations, experimental dose data were collected using instruments for measuring doses from electron, gamma and neutron radiation.

Chapter 2 begins with a summary of the basics of laser-plasma interaction and the mechanisms governing the acceleration process. Then follows a brief summary of the laser system at the Lund Laser Centre and an introduction to the cases to be investigated. This includes the geometry of the laboratory and some details of the properties of the accelerated particles that are produced.

Chapter 3 concerns radiation protection and the processes generating secondary radiation when the accelerated particles interact with the laboratory. A few quantities relevant to radiation protection and monitoring are summarized.

Chapter 4 describes the simulations within the scope of this thesis, beginning with an introduction of the GEANT4 class library, its functionality and how physical processes are handled. Then the specifics of the implementation in this project is presented. The chapter concludes with a description of the results from the simulations on deposited dose and the radiation flux in the laboratory.

In Chapter 5 the results of direct dose measurements are presented for the electron acceleration case where doses deposited from electrons and photons were registered. Here, a few different dosimetric instruments were used to get the effective dose at several locations in the laboratory. Simulations were then performed to mimic the measured case. The measured data is then compared to the simulated data.

Chapter 2

Laser-plasma acceleration

This chapter contains a summary of the basic laser-plasma interactions following expositions of Hansson (2016) [3] and Lundh (2008) [4]. Starting out with a section describing femtosecond laser pulses and fundamentals of lasers-plasma interaction. Following sections contains summaries of some of the mechanisms behind laser-driven particle acceleration through intermediate plasmas. Specifically *laser wakefield acceleration* for electron acceleration and *target normal sheath acceleration* for proton acceleration are described. The chapter concludes with specifics concerning the setups of the high-power laser facility at the Lund Laser Centre. Also the geometry and beam properties to be simulated are presented.

2.1   Laser field description

Propagation of light is governed by Maxwell's equations,

$$
\begin{cases}
\nabla \cdot \mathbf{E} & = \frac{1}{\epsilon_0} \rho \\
\nabla \cdot \mathbf{B} & = 0 \\
\nabla \times \mathbf{E} & = -\frac{\partial \mathbf{B}}{\partial t} \\
\nabla \times \mathbf{B} & = \mu_0 \left(\mathbf{j} + \epsilon_0 \frac{\partial \mathbf{E}}{\partial t} \right).
\end{cases}
\tag{2.1}
$$

Alternatively, the electric and magnetic fields can be related trough the electric scalar potential V and the magnetic vector potential $\mathbf{A}$ by,

$$
\begin{cases}
\mathbf{E} & = -\nabla V - \frac{\partial \mathbf{A}}{\partial t} \\
\mathbf{B} & = \nabla \times \mathbf{A}.
\end{cases}
\tag{2.2}
$$

Commonly, the normalized version of this vector potential,

$$
\boldsymbol{a} = \frac{e\mathbf{A}}{m_e c},
\tag{2.3}
$$

is then used to describe the laser field in laser-plasma interactions. The absolute value of the normalized vector potential may here be related to the intensity of a linearly polarized wave by

$$a_0 = \sqrt{\frac{e^2}{2\pi^2\epsilon_0 m_e^2 c^5}\lambda^2 I} \approx 0.85 \frac{\lambda}{1\,\mu\text{m}} \sqrt{\frac{I}{10^{18}\,\text{W/cm}^2}}. \qquad (2.4)$$

The transverse momentum of an electron is now approximately determined as $p_e \approx m_e c a_0$, becoming relativistic as a_0 approaches 1.

2.2 Plasmas

In the experiments described in this thesis, the plasmas are formed when laser light of sufficiently high intensity interact with the solid or gaseous matter in the target. The result of this is that the target atoms become ionized in the interaction. This means that a volume of unbound electrons and ions is formed, which as a whole constitutes a plasma. At this state of matter, electrons and ions interact with each other collectively, and in many cases share model properties similar to those found in fluid dynamics.

A fundamental criterion for a plasma is the ability of its constituent charges to redistribute themselves around an externally applied potential field. This gives the plasma a quasi-neutral behavior as local charge accumulations are shielded at a characteristic distance called the Debye length. Under the assumption that the mobility of ions are negligible compared to that of the electrons the *electron* Debye length, λ_D, can used to describe the plasma,

$$\lambda_\text{D} = \sqrt{\frac{\epsilon_0 k_B T_e}{n_e e^2}}, \qquad (2.5)$$

with electron temperature T_e and electron number density n_e. When electron motion can be approximated by a Maxwellian velocity distribution, then the electron temperature can be related to the average kinetic electron energy as $\langle E_\text{kin} \rangle = 3/2 k_B T_e$. The condition of quasi-neutrality is fulfilled when the length scales of the plasma is much greater than the electron Debye length, $l \gg \lambda_\text{D}$. The number of electrons within a sphere of radius λ_D is called the plasma parameter,

$$N_\text{D} = \frac{4\pi \lambda_\text{D}^3}{3} \cdot n_e, \qquad (2.6)$$

and must be large, $N_\text{D} \gg 1$, in order for the shielding to be effective.

2.2.1 Laser propagation in plasmas

For the time scales and field strengths we are concerned with, plasma ions are typically treated as an immobile background to the electron motion. A

few fundamental properties of light propagation in plasmas can be seen by considering plane electromagnetic waves of low intensities – which therefore only generate small perturbations of the plasma. Now, describing the electric field by a harmonic plane wave, $\mathbf{E} = E_0 \cos{(kx - \omega t)}\,\hat{\mathbf{x}}$ gives

$$\frac{\partial^2 \mathbf{E}}{\partial t^2} = -\omega^2 \mathbf{E} \tag{2.7}$$

$$\nabla^2 \mathbf{E} = -k^2 \mathbf{E}. \tag{2.8}$$

From the influence of the electric field, any displaced electrons will be subject to a force,

$$\mathbf{F}_{\mathrm{rest}} = m_e \ddot{\mathbf{r}} = -e\mathbf{E}, \tag{2.9}$$

with the current density being described by their radially outward flow, $\mathbf{J} = -en_e\dot{\mathbf{r}}$. This gives,

$$\frac{\partial \mathbf{J}}{\partial t} = \frac{e^2 n_e}{m_e}\mathbf{E} \tag{2.10}$$

Inserting equations 2.7–2.10 into the Maxwell wave equation with current term

$$\nabla^2 \mathbf{E} - \frac{1}{c^2}\frac{\partial^2 \mathbf{E}}{\partial t^2} = \mu_0 \frac{\partial \mathbf{J}}{\partial t}, \tag{2.11}$$

results in the relation

$$\omega^2 - c^2 \mu_0 \frac{e^2 n_e}{m_e} = k^2 c^2. \tag{2.12}$$

From here we can identify a plasma frequency,

$$\omega_p = \sqrt{\frac{e^2 n_e}{\epsilon_0 m_e}} \tag{2.13}$$

in order to identify a dispersion relation for electromagnetic waves in plasmas,

$$\omega^2 - \omega_p^2 = k^2 c^2. \tag{2.14}$$

The associated phase and group velocities of the waves are,

$$v_{\mathrm{phase}} \equiv \frac{\omega}{k} = \frac{c}{\sqrt{1 - \omega_p^2/\omega^2}} \tag{2.15}$$

$$v_{\mathrm{group}} \equiv \frac{\mathrm{d}\omega}{\mathrm{d}k} = c\sqrt{1 - \omega_p^2/\omega^2}. \tag{2.16}$$

From where it is seen that light propagates with phase velocities exceeding c inside the plasma, while the laser pulse itself has a (group) velocity below c.

An alternative view of the electron motion is achieved by considering the electric field created by the displaced electrons,

$$\mathbf{E}_{e^-} = -\frac{en_e\mathbf{r}}{\epsilon_0}, \tag{2.17}$$

which combined with equation 2.9 gives

$$\ddot{\mathbf{r}} - \omega_p^2 \dot{\mathbf{r}} = 0, \qquad (2.18)$$

so that the electron motion is seen to be described by an harmonic oscillator with the plasma frequency.

The plasma frequency now determines the natural oscillation frequency of the plasma – given its electron density n_e. For laser light with frequency lower than the plasma frequency ($\omega_l < \omega_p$) the dispersion relation 2.14 gives fully imaginary solutions of the wave vectors. This case is known as an *over-dense* plasma. Here, plasma electrons will effectively shield the laser field and hinder it from propagating. Instead the laser pulse is simply reflected back in the interaction.

Instead, for frequencies above the plasma frequency ($\omega_l > \omega_p$) the dispersion relation yield real-valued wave vectors and the plasma allows propagation of the laser light since the collective response from the plasma is slower than the laser oscillations. This is an *under-dense* plasma.

The transition frequency ($\omega_l = \omega_p$) is then the boundary for reflection of the incident light in a plasma and the associated electron density is denoted the *critical density* for that particular frequency,

$$n_c = \frac{\epsilon_0 m_e \omega_l^2}{e^2}. \qquad (2.19)$$

Instead, looking for purely longitudinal plasma waves we find that equations 2.7–2.11 yields,

$$\mu_0 \epsilon_0 \omega^2 \mathbf{E} = \mu_0 \frac{e^2 n_e}{m_e} \mathbf{E}. \qquad (2.20)$$

Non-trivial solution exist only for,

$$\omega = \sqrt{\frac{e^2 n_e}{\epsilon_0 m_e}} \equiv \omega_p, \qquad (2.21)$$

where we again find the natural oscillations of the plasma as seen in the dispersion relation 2.14. These purely longitudinal solutions do not have an associated dispersion relation and are called *electrostatic* plasma waves, or *Langmuir* waves. These waves are fundamental to the acceleration of electrons by means of laser wakefield acceleration – described in the following section where non-linear effects becomes apparent due to the higher laser intensities required.

2.2.2   Laser wakefield acceleration (LWFA)

In laser-plasma acceleration of electrons the so-called *laser wakefield acceleration* (LWFA) is the important acceleration mechanism. Here, a short and
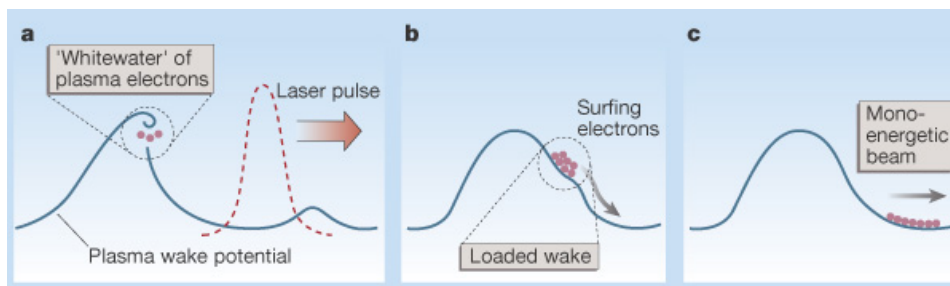
Figure 2.1: The principle of laser wakefield acceleration (LWFA) [5]. The laser pulse induces plasma density oscillations along the optical axis. As the amplitude of the oscillations gets large enough some plasma electrons deviates and gets trapped in the plasma potential and are accelerated.

intense laser pulse is made to interact with a gas target creating a plasma before the arrival of the peak of the laser pulse. The following interaction between the pulse peak and the under-dense plasma then pushes electrons forwards and outwards as the pulse propagates through the plasma. This results in the formation of a void of electrons (or *bubble*) which co-propagates with the laser pulse at a speed v_{group}. The electrons are pulled back by the restoring force of the positive charges left behind. This means that there is a formation of longitudinal plasma density variations along the optical axis. When the amplitude of these oscillations become sufficiently large, some of the plasma electrons will deviate from the collective motion described above and instead become trapped inside one of the plasma periods and therein be accelerated, cf. Fig. 2.1.

Ponderomotive force

An electron located in an optical field will undergo an oscillating motion due to the Lorentz force. For low intensities, the effect of the magnetic field can be neglected and the force takes the form

$$m_e \frac{\partial \mathbf{v}}{\partial t} \approx -e\mathbf{E} = -e\frac{\partial \mathbf{A}}{\partial t}. \tag{2.22}$$

If the electric field amplitude is varying along the path taken by the oscillating electron, the net momentum gained by the electron will be larger in one transverse direction and the electron will drift towards low-amplitude regions. This is a simple model of the ponderomotive force. In the case of a focused laser pulse this means that electrons will be pushed outwards from the optical axis and longitudinally away from the peak.

Following more complete derivations, the ponderomotive force can be

written in the non-relativistic regime as [3, 6]

$$\mathbf{F_p} = -\frac{q^2}{2\omega^2 m_e}\nabla\langle\mathbf{E}\rangle^2, \tag{2.23}$$

and in the relativistic regime as [3, 6]

$$\mathbf{F_p} = -\frac{q^2}{2m_e\langle\gamma\rangle}\nabla\langle\mathbf{A}\rangle^2, \tag{2.24}$$

where $\langle\cdot\rangle$ denotes the time-average over one period of the optical field. The overall effect of the ponderomotive force is therefore to push electrons forwards and outwards relative to the peak of a laser pulse.

Non-linear plasma waves

Given a plasma, due to the highly collective nature of the charge distribution the response to a laser pulse of high intensity will be the formation of non-linear waves in the plasma. Considering a one dimensional model, the response of the plasma to a laser pulse can be expressed as [3, 7]

$$\frac{\partial^2\phi}{\partial\xi^2} = \frac{k_p^2}{2}\left(\frac{1+a^2}{(1+\phi)^2} - 1\right), \tag{2.25}$$

where ϕ is the electrostatic potential of the plasma wave, and $\xi = x - v_{\text{group}}t$ the longitudinal coordinate in a frame co-moving with the propagation of the laser pulse. Shifts in plasma density δn from the unperturbed value n_0 are then closely related to the propagation of the electrostatic potential

$$\delta n/n_0 = \frac{1}{2}\left(\frac{1+a^2}{(1+\phi)^2} - 1\right). \tag{2.26}$$

By tuning the laser pulse duration appropriately given certain plasma parameters, resonances are formed which lead to a higher excitation of the plasma potential. For this to occur, the peak of the laser pulse should overtake the electrons that were initially pushed forward at the time they turn around due to the pull of the charge separation. This means that the ponderomotive force is in resonance with the restorative force of the charge separation.

Bubble regime

For laser pulses of high enough intensity, electrons will be completely expelled from a region in the plasma by the ponderomotive force. This causes the formation of an empty *bubble* in the electron density distribution, in the wake of the laser pulse. Large accumulations of electrons at the borders of the bubble give rise to large sudden changes in the electric field generated. This electric field inside the bubble is directed radially outwards from its center, accelerating bordering electrons towards it.

Electron acceleration

These models, describing the collective oscillations in a plasma, do not provide a mechanism for the net acceleration of electrons included in the oscillations. Instead, these excited plasma waves can only accelerate electrons belonging to a population of electrons that does not strictly obey the collective motion of the plasma but instead become trapped in the excited plasma wave.

As the amplitude of the plasma oscillations grows, *wave-breaking* can occur which puts an upper limit on the amplitude of the plasma oscillations. At these amplitudes, coherence in the collective motion is lost and the wave can start to break in a non-smooth way. A process called *self-trapping* can now occur. This happens when electrons that have broken off become trapped in the potential well of still oscillating plasma electrons. If this wave motion continues for long enough, trapped electrons may be accelerated to high energies [3].

2.3 Experimental setup

Here follows a summary of the laser system and experimental layout of the multi-terawatt laser at the Lund High-Power laser facility.

2.3.1 Lund high-power laser system

The multi-terawatt laser system at the Lund High-Power Laser facility is based on CPA (chirped pulse amplification) with Ti:sapphire as the amplifying medium throughout the system. A Kerr-lens mode-locked oscillator generates the seed laser light: a 80 MHz pulse train at a central wavelength of 800 nm and with a bandwidth of 50 nm. The duration of each pulse is below 20 fs and carries an energy of about 5 nJ. This train of pulses is fed through a Pockels cell pulse-picker which allows passage of 10 pulses per second. The light is then amplified up to a few µJ in a first amplification stage.

By introducing a approximately linear chirp, each pulse is stretched temporally before being amplified to a energy of about 1.5 J before compression, now with a pulse duration of approximately 450 ps. After amplification, the pulse is recompressed to below 40 fs. The stretching and compression of each pulse is achieved by gratings arranged such that the path length has a frequency dependency. In stretching, lower frequencies in the pulse will have shorter paths through the stretcher compared to higher frequencies which lead to a temporally drawn out pulse. In the compression stage this works, in reverse. The compression process introduces losses leading to pulse energies of approximately 1 J.

Since the laser cannot propagate in air under normal pressures, the experiments are performed in vacuum chambers, operating at pressures of 10^{-4} mbar or less). When the laser pulse reaches the target inside the vacuum

chamber it is focused, from a beam diameter of 60 mm, down to a beam diameter of a few microns (3–20 µm). The pulse length is about 40 fs and the energy content per pulse is after recompression below 1 J per pulse. The power of each laser pulse reaches up to about 20 TW, with peak intensities in the range $10^{18} - 5 \cdot 10^{19}$ W/cm^2 [3].

2.3.2   Rooms and vacuum chamber

Figure 6.1 shows the layout of the laboratory with the region simulated (cf. chapter 4) marked by a red outline. The outer radius of the chamber is 60 cm, with walls of 5 cm thickness and 35 cm in height. The thicknesses of chamber top and bottom are 5 cm and 10 cm, respectively.

A gas jet located in the center of the chamber is used as target for the laser pulse in the experiments on the laser wakefield acceleration of electrons. For the target gas, typically a hydrogen-nitrogen or hydrogen-helium mixture is used—with nitrogen at 1–2% of the total molecular count.

Implementation of the accelerated electrons

The accelerated electrons are implemented in the simulations as a beam originating from the center of the vacuum chamber, parallel with the "north"-direction in Figure 6.1. The beam radius is taken to be 2 µm at the source and has a divergence of 10 mrad (full-width at half-max).

The accelerated electrons are implemented as mono-energetic bunches in each simulation run. In order to build up data for a range of electron energies, the energy is changed in between runs.

Dipole magnet

A dipole magnet is used to resolve the energy of accelerated particles. The principle is illustrated in Figure 2.3. The deflection of a charged particle passing through the magnetic field will decrease with increasing particle energy, so that the exit point and angle of generated secondaries will be dependent on the energy of the primary particle (e) and must be accounted for in the simulations for more accurate particle trajectories.

In the electron acceleration setup, the dipole magnet has dimensions $(x, y, z) = (2.5 \, \text{cm}, 5 \, \text{cm}, 10 \, \text{cm})$ and an effective vector field in the x direction $\mathbf{B} = (0.65 \, \text{T}, 0, 0)$. Here, the optical axis is parallel to the z-axis. Because of the geometry of the dipole, electron energies above approximately 40 MeV can be resolved by this setup before clipping occurs as the deflected electron beam comes in contact with the magnet.

A particle with charge, q, traversing an electro-magnetic field at velocity,

v, will be exposed to a force described by the Lorentz force equation

$$\frac{d\mathbf{p}}{dt} = q(\mathbf{E} + \mathbf{v} \times \mathbf{B}), \tag{2.27}$$

where $\mathbf{p} = \gamma m \mathbf{v}$ is the particle momentum and the Lorentz factor is

$$\gamma = \frac{1}{\sqrt{1 - \beta^2}} = \frac{1}{\sqrt{1 - \frac{v^2}{c^2}}}.$$

Especially in the case of electron acceleration, the electrons are accelerated well up to relativistic energies of $K_e > 40\,\text{MeV}$ to a velocity $v_e > 0.9999\,c$.

Kinetic energies are here given by

$$K = mc^2(\gamma - 1) \tag{2.28}$$

and velocities may be directly obtained from the kinetic energy K as

$$\frac{v}{c} = \sqrt{1 - \frac{1}{\left(\frac{K}{mc^2} + 1\right)^2}}. \tag{2.29}$$

Classically, the deflection radius of a charged particle in a static uniform magnetic field is obtained from Eq. 2.27 by equating the centripetal force of the circular trajectory with radius r to the Lorentz force due to the magnetic field $\mathbf{B}$:

$$\frac{mv^2}{r} = qvB \quad \Rightarrow \quad r = \frac{mv}{qB}$$

Approaching relativistic energies, the momentum mv should be modified by γ such that the relevant expression becomes, in the electron case

$$r = \frac{\gamma mv}{eB} = \frac{p}{eB}. \tag{2.30}$$

Taking again the example of a 40 MeV electron; its trajectory will according to Eqs 2.29, 2.30 follow a circular path of radius $r \approx 0.2\,\text{m}$. For accuracy, it becomes necessary to implement a similar behavior in the following simulations. See section 4.5.2 for how the dipole magnets are implemented.
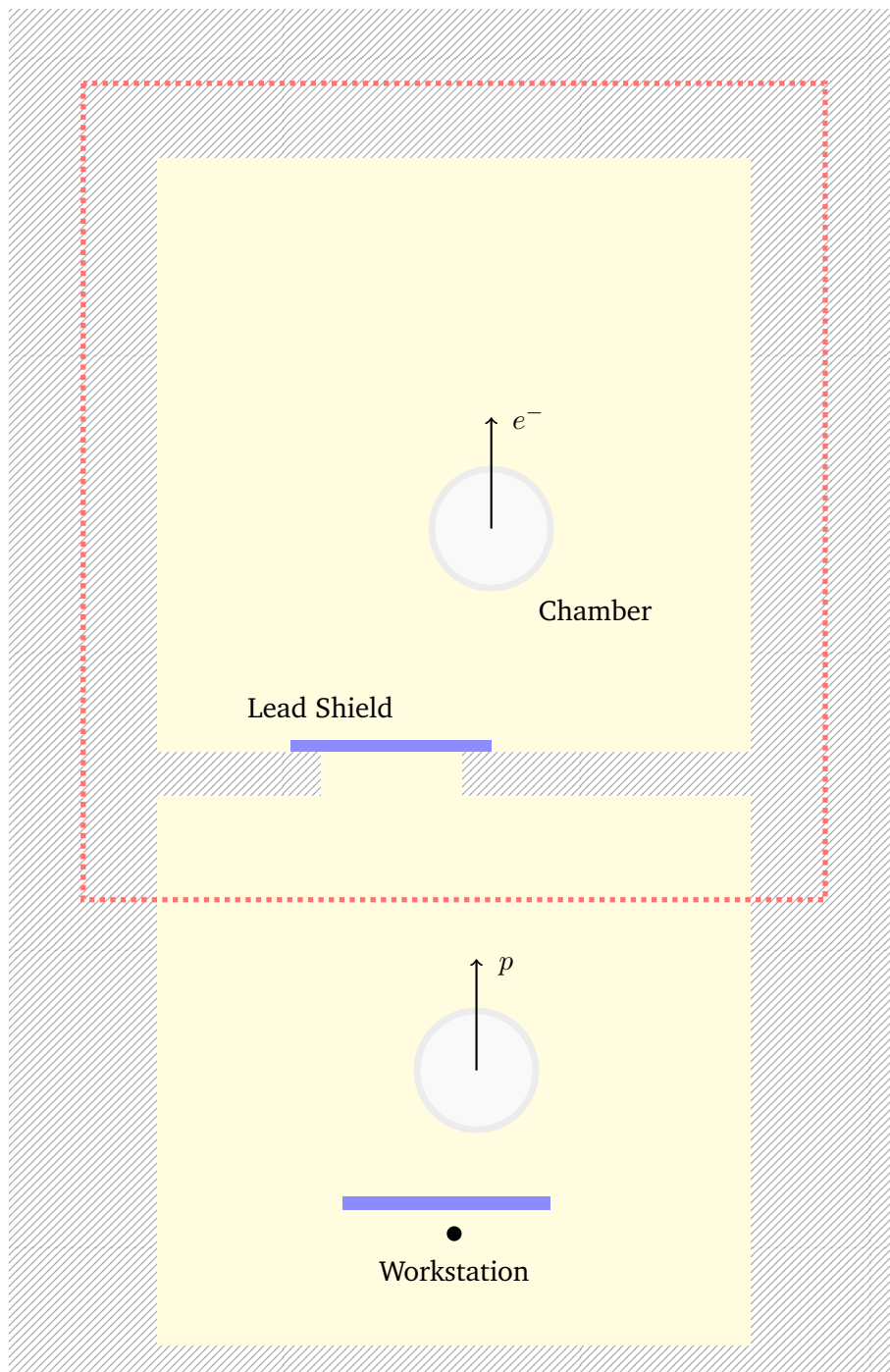
Figure 2.2: Layout sketch of the laboratory. The rectangle in red shows the region included in the simulations. Lead shields are drawn in blue; the upper one is a sliding door and here shown in its closed position. The position of the vacuum chambers are marked by grey circles, with the upper being used for electron acceleration.

Figure 2.3: Dipole magnet inside electron chamber: $0.65\,\text{T}$. The sketch shows the approximate deflection for a $40\,\text{MeV}$ electron inside the field. The trajectory draws a circle with radius $r \approx 0.2\,\text{m}$.

Chapter 3

Radiation protection and sources

3.1 Radiation quantities

For reference, this section contains the description of few physical and derived quantities with applications on radiation detection and radiation prot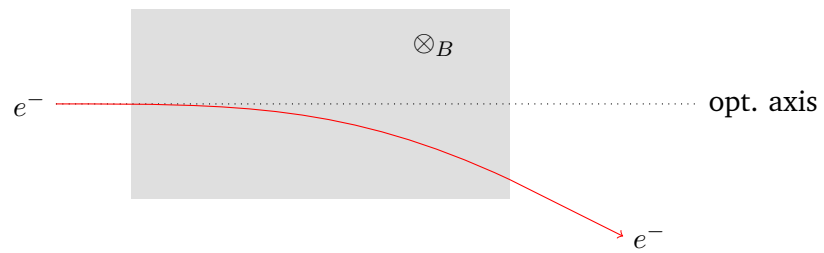ection. In the text below, *physical quantities* refers to quantities that are directly observable and that we are able to measure.

Protection quantities exist in order to quantify the damage to humans resulting from exposure to radiation. These protection quantities cannot be measured directly but are either derived from physical quantities or calculated through some approximative formulas depending on the biological material considered and the type and properties of an incident particle.

A third category, *operational quantities* are often used in providing conservative estimate of protection quantities, e.g. in dosimetric applications and area monitoring. Radiation protection equipment is often calibrated in terms of operational quantities.

3.1.1 Physical quantities

Fluence

Fluence (or flux) Φ [m^{-2}], is defined through the ratio

$$\Phi = \frac{dN}{da} \tag{3.1}$$

where dN is the number of particles passing through the infinitesimal cross-section da of a small sphere and is usually expressed in units of m^{-2} or cm^{-2}.

Fluence can also be equivalently expressed in terms of the path length dl with respect to a small volume traversed, dV [8],

$$\Phi = \frac{dl}{dV}. \tag{3.2}$$

Planar Fluence

Planar fluence (or *flat surface fluence*), is an alternative definition to the fluence described above. The surface is now a fixed plane and the planar fluence is then the number of particles dN crossing the surface per unit area da_{flat}. Since this surface has a fixed orientation, the particle fluence will now have to be modified with a factor $|\cos\theta|$ compared to the above fluence,

$$\Phi_{\text{flat}} = \frac{dN}{da_{\text{flat}}} = |\cos\theta| \cdot \Phi \tag{3.3}$$

with θ the incidence angle to the normal of the plane [8].

Since a cubic grid will be more efficiently implemented in a three-dimensional geometry, this quantity will be calculated to determine fluence in our simulations later.

Absorbed Dose

Absorbed dose, D $[1\,\text{Gy} = 1\,\text{J/kg} = 100\,\text{rad}]$, is given by

$$D = \frac{dE_{\text{dep}}}{dm} \tag{3.4}$$

where E_{dep} is the total energy deposited into a volume of a specific material with mass m [9]. The absorbed dose D is therefore the expectation value of the energy imparted per unit mass at a point.

More strictly, the quantity E above is called the *energy imparted*. It is defined in terms of energy difference between particles entering and exiting a volume,

$$E = R_{\text{in}} - R_{\text{out}} + \sum Q.$$

Here R_{in} and R_{out} is the *radiant energy* (energy exluding rest mass) and $\sum Q$ is the net energy change in rest mass entering and exiting the volume [8].

It is possible to relate absorbed dose to particle fluence Φ by approximate conversion coefficients (cf. section 3.2).

3.1.2   Protection quantities

Organ absorbed dose

Organ absorbed dose, D_T $[1\,\text{Gy}]$, in an organ or tissue T of mass m_T is given as the integral of the absorbed dose, D, over the mass of the organ:

$$D_T = \frac{1}{m_T} \int D\,dm$$

Table 3.1: Radiation weighting factors w_r (cf. eq. 3.5) for different types of radiation according to the two standards ICRP 60 [10] and ICRP 103 [11]. ICRP 60 only concerns protons with kinetic energy $E_p > 2\,\text{MeV}$.

| Radiation | | w_r | |
		ICRP 60	ICRP 103
photons	γ	1	1
electrons, muons	e^-, μ^-	1	1
neutrons	n		cf. Fig. 3.1
protons	p	5	2
charged pions	π^-, π^+	n/a	2
Alpha particles, heavy ions	α	20	20

Equivalent dose

Equivalent dose, H [Sv], in an organ or tissue gives a conservative correction to the absorbed dose D according to the potential harm done by a given radiation type. Equivalent dose is given as

$$H = \sum_r w_r D_r, \qquad (3.5)$$

where D_r is the absorbed dose D in a material equivalent to an average of human tissue from a specific radiation type r and w_r is a weighting factor depending on radiation type and energy [9]. In older literature w_r is denoted as the *quality factor*, Q, of a radiation type.

Table 3.1 lists weighting factors by radiation type for doses deposited in a human body analogue. These weighting factors are estimates recommended by the ICRP (International Commission on Radiological Protection) in the two reports; ICRP 60 [10] from 1990, and ICRP 103 [11] from 2007.

The potential damage done to tissue due to an incident neutron has a strong energy dependency with respect to other radiation types, and the conversion function is taken as a continuum with respect to neutron kinetic energy, see Figure 3.1. This come from which mechanism is dominant for the energy deposition process for a certain neutron energy. Around the peak at 1 MeV, elastic collisions producing secondary protons are more likely than the gamma producing mechanisms found at high energies (inelastic scattering) and low energies (neutron capture).

In the simulations (cf. chapter 4), doses are calculated by registering the absorbed dose D (the energy per volume mass deposited in some volume). Since recommendations on safe dose levels are usually given in equivalent dose H [Sv], the conversion from Gy to Sv should be done at runtime according to Figure 3.1.

The weighting factors based on ICRP 60 are valid legal EU regulations for calculating equivalent dose in organ or tissue. In accordance with the Euratom basic standards 1996 [12, 13], this will be repealed and replaced by the data based on ICRP 103 by 6 February 2018 [14].
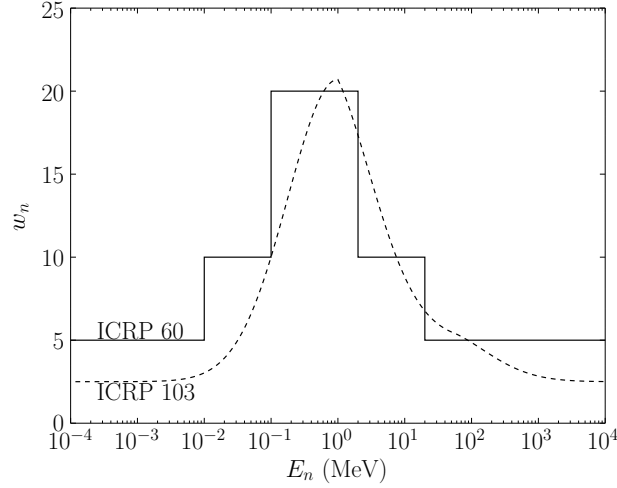

Figure 3.1: Neutron weighting factors w_n for conversion of absorbed dose D [Gy] into equivalent dose H [Sv] with E_n being the kinetic energy of incident neutrons. A peak around 1 MeV indicates a larger harm to biological tissue per energy absorbed relative to surrounding energies. Conversion factors from ICRP 60 [10], ICRP 103 [11].

Effective Dose

The effective dose, E [Sv], is the sum of equivalent doses to specific organs H_T, but now weighted according to the sensitivity of each organ relative to its mass density

$$E = \sum_T w_T H_T, \qquad (3.6)$$

where the weighting factors for all organs sum up to unity, $\sum_T w_T = 1$.

For clarity the effective dose E can therefore be expressed directly in terms of absorbed dose D_T as,

$$E = \sum_T w_T \sum_r w_r D_T.$$

For completeness Table 3.2 lists specific values for the tissue weighting factor w_T for different organs [10, 11].

Table 3.2: Weighting factors for different tissues. Values of w_T from ICRP 60 and ICRP 103 [10, 11].

| | w_T | |
Tissue	ICRP 60	ICRP 103
Gonads	0.20	0.08
Red bone marrow	0.12	0.12
Colon	0.12	0.12
Lung	0.12	0.12
Stomach	0.12	0.12
Breasts	0.05	0.12
Bladder	0.05	0.04
Liver	0.05	0.04
Esophagus	0.05	0.04
Thyroid	0.05	0.04
Skin	0.01	0.01
Bone surface	0.01	0.01
Salivary glands	–	0.01
Brain	–	0.01
Rest of body	0.05	0.12

3.1.3 Operational quantities

Instruments used in dosimetry are usually calibrated in terms of a *operational quantity*, which give conservative (high) estimates for the equivalent dose that would have been deposited in tissue. One example is the *personal dose equivalent*, $H_p(d)$ [Sv], which is a measure of the equivalent dose at a depth, d, into the human body. Typically, personal dosimeters are calibrated in this quantity and it is therefore the operational quantity for individual monitoring. The actual measured dose at a small volume in space is therefore calibrated to represent a small section of the human body at depth d.

To assess the *effective dose* inside the human body, the quantity $H_p(10)$ with a depth $d = 10\,\text{mm}$ is often used for calibration of instruments. For assessing doses to skin, hands and feet, the quantity $H_p(0.7)$ with a depth $d = 0.7\,\text{mm}$ is used. [9].

3.2 Dose conversion coefficients

Given the flux of a radiation type, it is possible to convert directly to dose deposited in a certain material. In the simulations described in chapter 4, this will be used to reduce computational time in building a map of the potential
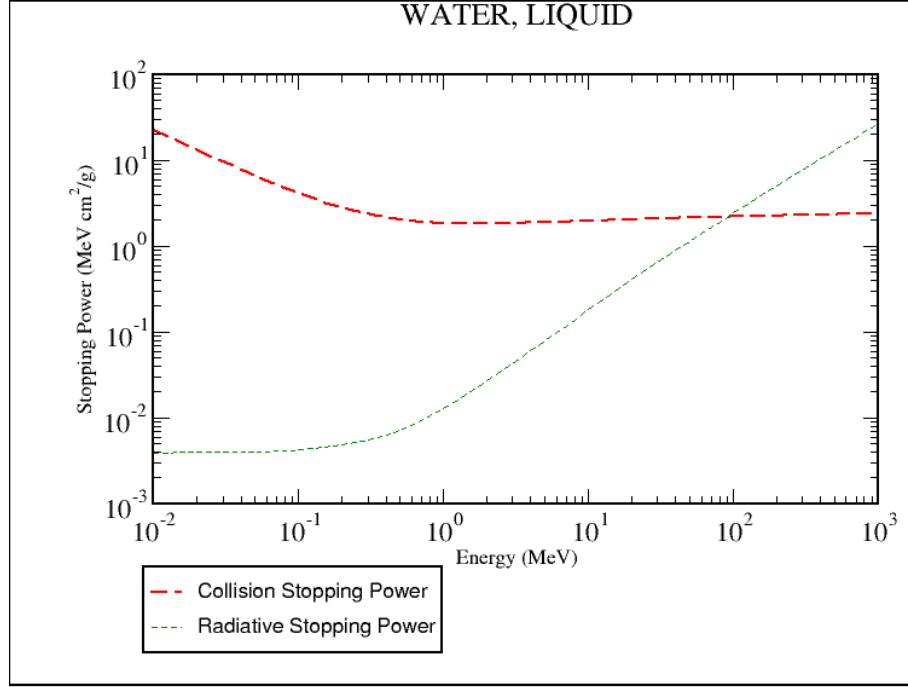
Figure 3.2: Collisional and radiative stopping power of water [16].

equivalent doses deposited for the geometry of the laboratory.

3.2.1 Electron flux to dose

Electrons depositing energy directly into a body will do so through collisional (elastic) processes. To determine the dose deposited in this manner from the electron fluence, Φ_e, it is possible to make use of the collisional stopping power component, S_{coll} of Bethe's stopping power formula [15], to get the expression,

$$H_{e^-} = \Phi_e \frac{S_{\text{coll}}}{\rho}. \tag{3.7}$$

Here ρ is the density of the absorbing material and the collisional stopping power, S_{coll}, is given for a specific absorber material using ESTAR (stopping-power and range tables for electrons), NIST [16], cf. Fig. 3.7.

3.2.2 Photon flux to dose

Equivalent dose H_γ deposited by photons can be determined from the fluence Φ as

$$H_\gamma = \Phi_\gamma E \frac{\mu_{\text{en}}}{\rho}, \tag{3.8}$$

24

where E_γ is the photon energy, ρ is the density of the absorbing material and μ_{en}/ρ is the *mass-energy absorption coefficient* (unit: cm^2/g), which is dependent on absorbing material and the photon energy [17]. Data for μ_{en}/ρ taken from NIST [18, 19].

3.2.3 Neutron flux to dose

Absorbed dose from neutrons are determined directly from conversion factors which are a combination of experimental and simulated data. Figure 3.3 shows conversion factor from neutron fluence, Φ, to equivalent body dose, H, based on simulation data [20] with data for neutron energies from Leuthold et al. (1992) [21] and with absorbed dose to equivalent dose conversion factors from ICRP 60 [10].

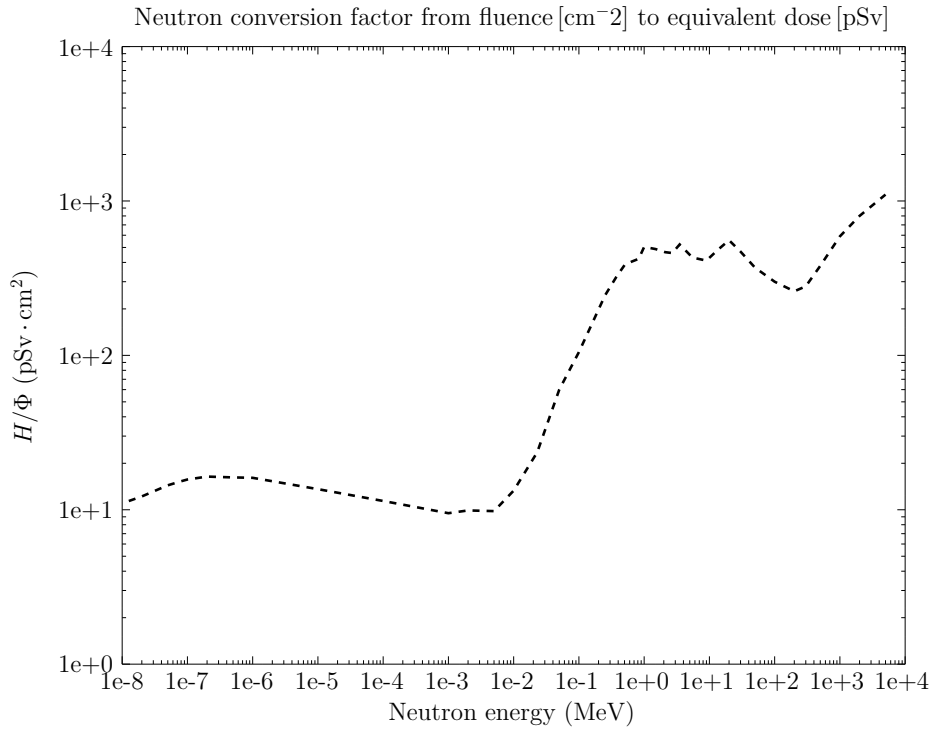Figure 3.3: Conversion factors from neutron fluence Φ [cm^{-2}] to equivalent body dose H [pSv].

3.3 Health effects

The effects of radiation on living tissue are categorized as either *stochastic effects* or *deterministic effects*.

Stochastic effects are associated with lower dose-rates and involve reactions which are not directly observable but where genetic material is damaged such that cell mutations may occur. This can give rise to formation of cancers or if mutation occurs in the reproductive cells to heritable mutations being passed on to children. The occurrence of cancers due to stochastic effects commonly modeled by a linear relationship to equivalent dose–an accumulation of 1 Sv dose over time corresponding to a 5.5 % probability of cancer being induced [11].

The class of deterministic effects involves higher dose rates where the direct induction of cellular failure, e.g., by breaking apart genetic material so that reproduction is halted or damage of molecular structures in the cell causing it to malfunction. For full body absorbed doses on the order of 1 Gy over a couple of hours this may lead to *acute radiation syndrome* with risk of severe radiation damage [11].

3.4 Recommended dose limits

In order to minimize the impact of stochastic health effects, to persons conducting a practice involving ionizing radiation, the Swedish Radiation Safety Authority (Strålskyddsmyndigheten) puts a full body effective dose limit at 50 mSv for any one given year. In addition, for any given 5 year period the effective full body dose should not exceed 100 mSv, giving an effective maximum dose at 20 mSv per year [22, 23].

Other limits for whole body dose are: by CERN 15 mSv/yr^{-1}, in the U.K. 15 mSv/yr^{-1} and in the U.S. 50 mSv/yr^{-1} [9].

3.5 Radiation sources

Here follows a description of the primary sources for radiation generation for the energies considered in this project.

3.5.1 Bremsstrahlung

At the particle energies achieved in the experiments on laser wakefield acceleration the primary interaction for a beam of electrons with surrounding matter is by bremsstrahlung. Bremsstrahlung occurs when an incident electron scatters off an electric field in a target nucleus (and to a lesser extent by the electric fields of the atomic electrons surrounding the nucleus). The incident electron loses some of its energy through intermediate photon-interaction with the nucleus and produces a free photon in the process. The photons produced follow a synchrotron-like energy distribution and may have an energy up the initial energy of the electron. The slowed down electron may in turn undergo secondary bremsstrahlung interactions [24].

Figure 3.4 shows the lowest order Feynman diagrams for the bremsstrahlung process, where an incident electron interacts with the electric field of a nucleus through an intermediate exchange photon,

$$e^- + (Z, A) \longrightarrow e^- + \gamma + (Z, A).$$

The probability for this process to occur is proportional to the square of the atomic number, $p_{\text{nuclear}} \sim Z^2$. There is also a possibility that the incident electron will undergo bremsstrahlung production by interacting with the atomic electrons. This probability of this process scales linearly with atomic number, $p_{\text{atomic}} \sim Z$, which quickly makes it insignificant, in comparison to bremsstrahlung due to the nucleus, even for moderately heavy elements [25].

The secondary photon produced may in turn interact with the surrounding material to undergo other radiation inducing processes (see below).
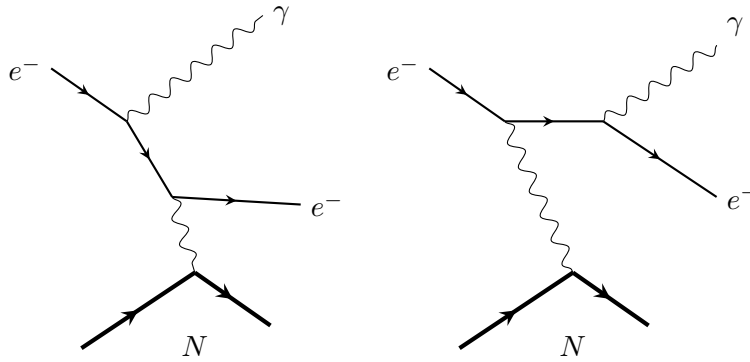

Figure 3.4: The dominant bremsstrahlung processes, illustrated as Feynman diagrams, where an incident electron scatters off of a nucleus, N, resulting in the production of a free photon.

3.5.2 Pair production

Electron-positron pair production

Photons originating from the primary bremsstrahlung processes may in turn undergo secondary interactions. For photon energies above $1.022\,\text{MeV}$ the production of an $e^- e^+$ pair may occur by scattering in the vicinity off the Coulomb field of a target nucleus, cf. figure 3.5 [25, 26].

It is also possible for the photon to interact with the Coulomb field of one the electrons surrounding the nucleus, resulting in a process emitting two electrons and one positron. Here, the electron-positron pair is created just as before, but the host electron, whose field the photon scattered from, is also ejected. This case is called *triplet production* and it has a higher reaction threshold of $E_\gamma = 4m_e = 2.044\,\text{MeV}$, needed to satisfy momentum conservation.

The atomic cross-section, σ_{triplet}, of triplet production (for all atomic electrons combined) is still small compared to the nuclear pair production, σ_{pair}. Their relative importance can be approximately given by,

$$\frac{\sigma_{\text{triplet}}}{\sigma_{\text{pair}}} \simeq \frac{1}{CZ},$$

for a target with atomic number Z and where C is a parameter which only depends on $h\nu$. $C = 1$ for $h\nu \to \inf$ and rises slowly to $C \to 2$ at $5\,\text{MeV}$. So that triplet-production will in general have a small contribution to $e^- e^+$ radiation produced [8].
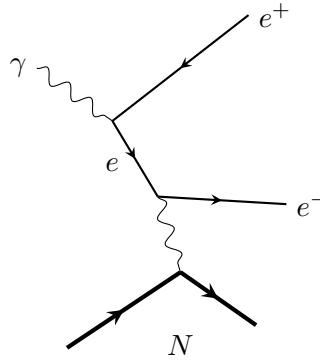

Figure 3.5: Pair production in the case of $(\gamma, e^+ e^-)$. There also exists an equally significant process where e^- and e^+ are swapped. Similar diagrams can be also drawn for the muon pair production, $(\gamma, \mu^+ \mu^-)$.

Muon pair production

The production of a $\mu^- \mu^+$ pair similar process to the $e^- e^+$ pair production. Because of the heavier muon this process has an energy threshold of $E_\gamma \leq 2m_\mu \approx 211\,\text{MeV}$ (the muon rest mass is, $m_\mu = 105.66\,\text{MeV}$) [26].

This process is, however, unlikely for the electron energies currently achieved and start to contribute at energies above $1\,\text{GeV}$ and behind the beam dump [27].

3.5.3 Neutrons

The production of neutrons becomes possible when a photon of a few MeV excites a nucleus by various photo-nuclear processes. In the case of accelerated electrons interacting with media the production of neutrons under photo-nuclear processes becomes relevant above electron energies of about $10\,\text{MeV}$ [8]. Because photons have much larger nuclear cross-sections compared to electrons, these photo-nuclear processes are the dominant processes

in producing radiative neutrons and other particles that are a result of inelastic nuclear reactions [26].

Neutrons are very efficient at depositing their energy in water, due to collisional effects with the hydrogen nucleus, and can therefore be particularly harmful to humans [9]. Besides this, generated neutrons may activate their surroundings (and in our case the hardware of the accelerator setup) especially in the target region, inducing radioactive decay processes.

Giant Photo-Nuclear Resonance

The giant photo-nuclear resonance is the dominant photo-nuclear process for neutron production. The interaction probability is peaked around 20–23 MeV for light nuclei ($A < 40$) and at 13–18 MeV for heavier ones [27].

The process consists of two steps: first the nucleus as a whole is excited by photon absorption, subsequently de-excitation by neutron emission occur. The probability of these resonant processes with respect to energy typically takes the form of one large peak, but for some nuclei several peaks will appear [26].

Pseudo-deuteron Production

For higher photon energies of about $30 - 300$ MeV, the incoming photon is more likely to enter resonance processes directly with a proton-neutron pair (a pseudo-deuteron) than with the nucleus as a whole. A neutron is then produced in the subsequent breakup of the pseudo-deuteron [26, 27].

Chapter 4

Simulations in GEANT4

GEANT (*Geometry And Tracking*) is a C++ class library for general purpose particle tracking [1, 2]. The program has grown out of collaborations mainly centered at CERN, available at geant4.web.cern.ch/geant4/. For the simulations presented in this work, the version GEANT4-10.2.1 has been used.

Electrons are typically accelerated to hundreds of MeV while protons are accelerated to below 10 MeV. Due to the the higher repetition rates at higher energies, we choose to focus on electron acceleration in the following simulations.

4.1 Monte Carlo engine

GEANT utilize Monte Carlo methods in order to introduce stochastic variance into the simulations. In GEANT this means that for each step in a particle interaction process all possible events are given a weight according to their relative probabilities. Then a random number generator is used to pick one event from distribution of possible events.

The Monte Carlo engine used is named `RanecuEngine` in GEANT. Its generation of pseudo-random numbers is based on combining several *multiplicative linear congruential generators* [28] in the, so called algorithm of l'Ecuyer [29].

A *linear congruential generator* (LCG) is defined by the property that numbers are generated through an expression of the form

$$s_{i+1} = (as_i + b) \bmod m, \tag{4.1}$$

where the *modulus* m and multiplier $a < m$ are positive integers and the constant b is a non-negative integer. The number s_0 is called the *seed* of the generator and m modulus of the generator. Pseudo-random numbers $g(s)$ are then generated by the sequence $g(s_i) = f(s_i)/m$. A common choice is to make $b = 0$, in which case the generator is called a *multiplicative linear congruential generator* (MLCG) [28].

In order to ensure that individual runs have minimal correlation between each other, a pair of seed numbers fed to the random engine can be set differently at the start of each run. The code following this section ensures that the seeds are changed automatically for each run. The function `BeginOfRunAction()` in `RunAction.cc` is called at the start of each run (see later following sections for details). From the `<time.h>` library the function `time(NULL)` returns the current Unix (POSIX) time in seconds, which is the number of seconds elapsed since time 00:00:00 (UTC), 1 January 1970 (leap seconds excluded). For example, at the time of writing `time(NULL)` returns `1462653153`. This is the `systime` and is taken as one of the two seeds for the random-engine. The other seed is created by multiplying `systime` by number generated from a uniform random distribution. Finally, the seeds are fed to the random-engine by G4Random::setTheSeeds().

```
//RunAction.cc
#include "Randomize.hh"
#include <time.h>
(...)
void RunAction::BeginOfRunAction(const G4Run*)
{
  // set random seeds from system time
  long seeds[2];
  long systime;
  systime = time(NULL);
  seeds[0] = (long) systime;
  seeds[1] = (long) (systime*G4UniformRand());
  G4Random::setTheSeeds(seeds);
  (...)
}
```

4.2 Role of core Classes

This section summarize the basic operation of the main classes for implementation and initiation of geometry and physics to be simulated.

4.2.1 Main

The class `Main.cc` handles the setups of the random engine used and initializes G4RunManager which manages the procedures of a run.

```
G4Random::setTheEngine(new CLHEP::RanecuEngine);
G4RunManager* runManager = new G4RunManager;
```

Then, new instances of the classes handling geometry and physics are created and initialized by calls to SetUserInitialization() in G4RunManager

```
DetectorConstruction* det= new DetectorConstruction;
runManager->SetUserInitialization(det);

PhysicsList* phys = new PhysicsList;
runManager->SetUserInitialization(phys);
```

Also creates a new instance of `G4UImanager` which handles user input at run time. Typically this is done in batch mode where the input is one or more *macro* (.mac) files which contain a list of commands for quickly changing simulation parameters and properties of the particle source.

4.2.2 DetectorConstruction

The class `DetectorConstruction.cc` defines the materials used in the geometry. This can be done in two different ways. The first way is to explicitly construct the material from its elements, as shown in the listing below for water.

```
G4Element* H = new G4Element("TS_H_of_Water" ,"H" , 1., 1.0079*g/mole);
G4Element* O = new G4Element("Oxygen"      ,"O" , 8., 16.00*g/mole);

G4int ncomponents, natoms;
G4Material* H2O =
        new G4Material("Water_TS", 1.000*g/cm3, ncomponents=2,
                                          kStateLiquid, 293*kelvin, 1*bar);
        H2O->AddElement(H, natoms=2);
        H2O->AddElement(O, natoms=1);
        H2O->GetIonisation()->SetMeanExcitationEnergy(78.0*eV);
```

The second way to create an instance of a material is to use the `G4NistManager` class to retrieve one of several materials from a database of materials [30]. This is shown in the listing below for concrete.

```
G4NistManager* man = G4NistManager::Instance();
G4Material* concrete = man->FindOrBuildMaterial("G4_CONCRETE");
```

After these materials are defined, the geometry is built either from a combination of instances of GEANT4 predefined solids (boxes, cylinders etc.) or by creating a mesh from a CAD model. A material is then assigned to each solid and it's position in the world geometry is defined.

In this project, only the vacuum chamber is implemented using a CAD model. This is done in the following way using CADMesh [31].

```
G4VSolid * cad_solid;
G4LogicalVolume * cad_logical;

CADMesh* mesh = new CADMesh("Chamber.stl", m,
                G4ThreeVector(0,-33*cm,0), false);
```

```
cad_solid = mesh->TessellatedMesh();
cad_logical = new G4LogicalVolume(cad_solid,
CylMaterial, "cad_logical", 0, 0, 0);

G4RotationMatrix* yRot2 = new G4RotationMatrix;
yRot2->rotateY(M_PI/2.*rad);

new G4PVPlacement(yRot2, G4ThreeVector(), cad_logical,
                  "cad_physical", lWorld, false, 0);
```

4.2.3 PhysicsList

In `PhysicsList.cc` all particle types and physical processes present in the simulations are defined.

GEANT allows one to use so called *reference physics lists* for implementing physical processes that should be available in the simulations. These are full physics lists, constructed for certain simulation purposes (e.g. radiation protection, high-energy particle interactions). The reference physics lists are continuously maintained and validated by the GEANT community and recommended for this reason.

The physical processes implemented in the current simulations are based on the reference physics list `QGSP_BERT_HP` which has here been modified to include `G4EmStandardPhysics_option4`, cf. section 4.6, which replaces the standard package for electromagnetic physics and uses more accurate models especially for the initial bremsstrahlung interactions [32]. The choice of `QGSP_BERT_HP` follows recommendations by GEANT project maintainers for use in dosimetric and shielding applications and allows tracking of neutrons down to thermal energies [33].

The below listing shows the processes being registered to the `RunManager` from inside `PhysicsList.cc`.

```
// Hadron Elastic Scattering
RegisterPhysics(new G4HadronElasticPhysicsHP(verb));

// Hadron Inelastic Scattering
RegisterPhysics(new G4HadronPhysicsQGSP_BERT_HP(verb));

// Ions
RegisterPhysics(new G4IonPhysics(verb));

// Gamma-nucl.
RegisterPhysics(new G4EmExtraPhysics());

// Electromagetic
RegisterPhysics(new G4EmStandardPhysics_option4());

//Stopping
RegisterPhysics(new G4StoppingPhysics());
```

```
// Decay
RegisterPhysics(new G4DecayPhysics());
```

4.3 Structure of a Run

In GEANT4, a *run* is the largest unit of simulation and consists of a collection of *events* realated to the same geometry and physics conditions. The run is represented by an instance of the `G4Run` class and starts with the `BeamOn()` method in `G4RunManager`.

One *event* is in turn represented by the `G4Event` class. It contains a stack of primary *tracks* managed by `G4EventManager` which are tracked (see below) one by one, any secondary tracks are pushed back into the stack. The event is over when the stack is empty.

A *track* is a representation of the current state of a particle as an instance of the `G4Track` class. At the beginning of processing a track, an instance of `G4TrackingManager` receives a primary track from the event manager and takes the actions to finish tracking it, which is performed by *stepping*.

One *step* is represented by `G4Step` and contains the points in the geometry before and after the step, together with its associated energy loss and time-of-flight. An instance of `G4SteppingManager` determine each step from the geometry and possible matter interactions and updates the relevant track, possibly killing it, inducing a particle change and/or producing secondary tracks [32].

4.4 Implementation of beam of accelerated electrons

The properties of the accelerated electrons are set to the general particle source in the .mac-file used. The code snippet below shows the implementation of a 1 pC electron pulse at 100 MeV, originating from a disc of 2 μm and with a Gaussian angular distribution of 10 mrad (FWHM).

```
% Particle type
/gps/particle e-

% Origin to be a circle of radius 2 micro-meter
% at centre of world volume
/gps/pos/shape Circle
/gps/pos/centre 0. 0. 0. mm
/gps/pos/radius 2. um

% Set the angular distribution as a Gaussian with 10 mrad (fwhm)
% around the propagation direction (positive z in world coordinates).
/gps/ang/type beam1d
/gps/ang/sigma_r 0.00425 %10 mrad FWHM
```

```
% Uniform energy distribution
/gps/ene/mono 100 MeV

% Generate number of electrons equivalent to a 1 pC pulse
/run/beamOn 6241509
```

4.5 Geometry

The geometry is defined in `DetectorConstruction.cc` as described above. GEANT4 requires three steps in creating a physical body with which particles may interact. Its geometrical shape and dimensions are defined, typically using some pre-defined class derived from `G4Solid`. Examples of classes inheriting from `G4Solid` are instances of `G4Box` (a box), `G4Tubs` (a hollow or solid cylinder, and `G4Sphere` (a sphere). A logical volume is created as a new `G4LogicalVolume` object. The importance of this logical volume is to define material properties and assign it to the solid. The object is placed in the geometry as a new instance of the `G4PVPlacement` class. To do this, the global coordinates of the volume are specified together with the mother volume in which it is contained. The exception is the world volume, which has no mother volume.

4.5.1 Chamber geometry

The vacuum chamber, in which the laser-plasma interactions take place, is implemented in the simulations using a CAD model of its essential geometry, cf. figures 4.1, 4.2 for the STL-file used. Using the program CADMesh [31, 34], the CAD model is converted into a collection of GEANT4 solids at compilation time.

The material of the chamber is aluminum, which has a ready implementation in the GEANT4 materials database as `G4_Al`.

4.5.2 Dipole Magnet

As mentioned above in section 2.3.2, a static dipole magnet is used in the experimental setup to resolve the energy distribution of a pulse of generated particles. This is the main mode of operation for the setup and should be accounted for.

This is implemented at the time of constructing the geometry. The listing below includes the relevant code in `DetectorConstruction.cc` for defining the magnetic field.

```
//DetectorConstruction.cc
#include "G4UniformMagField.hh"
```
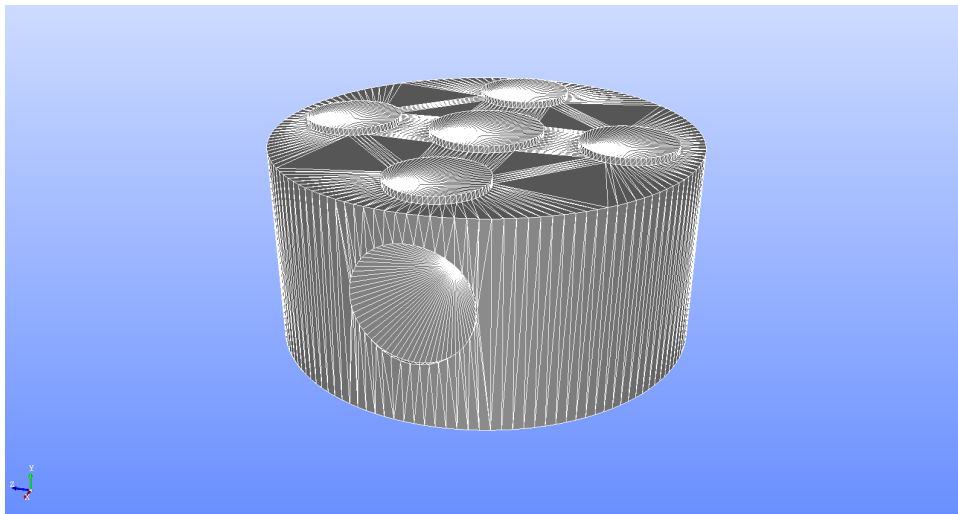
Figure 4.1: Chamber CAD model as described in a STL-file viewed graphically. The primary electrons to be tracked propagate from the center of the chamber towards the circular flat plate in the front of the chamber.
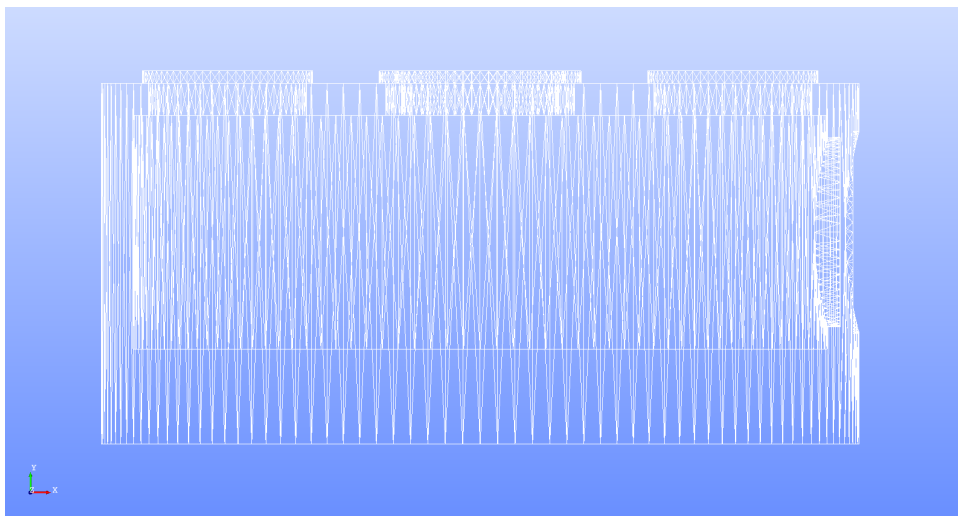

Figure 4.2: Chamber CAD model as an STL-file, side view. The chamber walls have thickness 5 cm except in the direction of electron propagation where it instead is a circular flat plate of 2 cm thickness with interfaces to connect the internal instruments in the chamber to the outside.

```
#include "G4FieldManager.hh"
(...)
G4Box
    *sMagField = new G4Box( "solid_magfield", 2.5/2*cm, 5/2*cm, 10/2*cm);
G4LogicalVolume
```

```cpp
    *lMagField = new G4LogicalVolume(sMagField, fWorldMat, "logical_magnet");

G4ThreeVector fieldValue = G4ThreeVector(0.65*tesla,0,0);
G4UniformMagField *magField = new G4UniformMagField(fieldValue);

G4FieldManager *fieldMgr = new G4FieldManager(magField);
fieldMgr->SetDetectorField(magField);
fieldMgr->CreateChordFinder(magField);

//accuracy mag.
G4double minEps= 1.0e-5; // Minimum & value for smallest steps
G4double maxEps= 1.0e-4; // Maximum & value for largest steps

fieldMgr->SetMinimumEpsilonStep(minEps);
fieldMgr->SetMaximumEpsilonStep(maxEps);
fieldMgr->SetDeltaOneStep(0.5*um); // 0.5 micrometer

lMagField->SetFieldManager(fieldMgr, true);

new G4PVPlacement(0, G4ThreeVector(0,0,18*cm), lMagField, "Magnet",
                  lWorld, false, 0);
```

In order to implement the magnetic field, a G4Box is first defined with
dimension given in x, y and z directions. Then, a logical volume is registered
to the solid. This is made up of the same material as the world volume – air
at a pressure of 1×10^{-5} Pa.

Then, the magnetic field is created by passing a vector with the x, y and z
components of the **B**-field to an instance of the class G4UniformMagField().
A new instance of the class G4FieldManager() then registers the magnetic
field to the logical volume. After this, boundaries for the step lengths inside
the magnetic fields are set. Finally the volume is placed as a physical volume
inside the world volume.

4.6   Physical processes

All physical processes available in the simulation must be defined and ini-
tialized using a collection of *physics contructor classes*. Here, each class
corresponds to a single process and defines its cross-section using theoretical
models or experimental data sets, the energy range where the process is
available and the associated particles involved.

A convenient way to implement a full collection of physics processes is to
construct a *physics list* which constructs processes by loading pre-packaged
modules of all physics contructor classes for a certain type of interaction, e.g.,
electro-magnetic, photo-nuclear, hadronic elastic/inelastic interactions etc.

Appendix A contains details of the physics models used in the QGSP_BERT_HP
model and G4EmStandardPhysics_option4 (included in PhysicsList.cc, cf.
section 4.2.3) are presented. QGSP_BERT_HP is the recommended starting

point for radiation analysis from electromagnetic processes and where neutrons are tracked down to thermal energies [33].

4.6.1 Production thresholds

Some electromagnetic processes, e.g., bremsstrahlung, leads to a particle cascade in which an immense number of secondaries with lower and lower energy are being produced for each step in the cascade. It is computationally unfeasible to keep track of all secondaries being produced in this way, and in order to avoid it, these processes require limits for the continued production of secondary particles (gammas, electrons, positrons). These limits are specified as a range called a production cut and is given in length units. This is the suggested minimum step length for a particle inside the given material. For each given material, the production cuts are then converted into minimum kinetic energies for each particle, above which it will continue to produce secondaries to be tracked.

By default, production cuts in GEANT4 are set to 0.7 mm. GEANT has a minimum production energy of 0.99 keV for all above particles which sets the lower limit on the conversion from production cuts (given in length units) to production energy. Since the primary interaction of the electrons generated is through bremsstrahlung, the accuracy in the current simulations are improved setting the production cuts to a lower limit. A value 0.1 mm was used, which was reached by trial and error. Below this value the time of a single run became unreasonably large. Table 4.1 shows the production limits in energy for production cuts of 0.01 mm, 0.1 mm and 0.7 mm for the materials involved in the simulation.

Below the production threshold the primary particle will not generate secondaries according to the relevant electromagnetic processes—but all particles are at all times tracked to zero energy, so the choice of production cuts will not affect the total energy deposited by the primary. The difference is that particles below the production cut will lose their energies in the simulations continuously rather than in a discrete manner when production of secondaries occur. The stopping location for a given particle is still correct regardless of production cuts chosen [32].

4.7 Collection of simulated dose data

This section introduces the methods used for collection of accumulated dose. This is done in two ways: first by directly recording the energy deposited in water phantoms which are placed (1) in the beam and directly outside the the room containing the chamber with (2) lead screen open and (3) lead screen closed. In this case doses are generated from simulation of electron beam energies ranging from 10 MeV to 2000 MeV.

Table 4.1: Limits [keV] for electrons (e^-), positrons (e^+) and gammas (γ) to produce secondaries in concrete, aluminum and lead

	e^-			e^+			γ		
[mm]	0.01	0.1	0.7	0.01	0.1	0.7	0.01	0.1	0.7
conc.	32.8	124	434	32.4	123	419	0.99	2.01	4.90
Al	34.2	131	460	33.9	128	442	0.99	2.35	5.86
Pb	58.1	242	1004	57.0	232	951	6.00	29.5	94.6

Secondly, maps of doses for electron beam energies of 100 MeV, 500 MeV, and 1000 MeV are calculated from particle flux and energy using a mesh defined over the whole simulated region.

4.7.1 Water phantom

Doses are calculated directly using `G4DoseDeposit.cc`, which collects doses deposited for each step in a predefined region by calling `GetTotalEnergy Deposit()` at each step taken. This is divided by the mass of the defined absorbing volume and from there returns the absorbed dose [Gy]. In order to get the equivalent dose [Sv] `G4DoseDeposit.cc` has been modified to include conversion factors for neutron dose [Sv] depending on their energy. Here, conversion factors from ICRP 60 [10] as previously presented in section 3.2 have been used. The choice of ICRP 60 over ICRP 103 for neutron conversion factors is motivated by the following section on building dose maps of the laboratory geometry, which uses data for neutron flux to dose conversion which partly builds upon ICRP 60. The differences inbetween the two standards are negligible for the accuracy required (cf. Fig. 3.1).

4.7.2 Dose map from particle flux

In order to build a map over doses in the laboratory geometry, particle fluxes were collected by the GEANT4 class `G4PSFlatSurfaceFlux.cc`, which allows one to specify a mesh of surfaces on a rectangular grid and then collects particles passing through each surface and computes the flux (in cm^{-2}) [32]. The mesh of surfaces was defined to cover the whole floor area of the laboratory with a single 60 cm mesh layer built up of cells with sides $(\Delta x, \Delta y, \Delta z) = (2\,\text{cm}, 60\,\text{cm}, 2\,\text{cm})$. The center of the mesh was aligned in height with the center of the chamber.

In order to get tissue equivalent dose levels from collected fluxes, `G4PSFlatSurfaceFlux.cc` was modified to rescale the flux collected for a given particle type (e^-, γ or n) with the corresponding conversion factor for its kinetic energy, as given in section 3.2.

In this way, we will be able to build a map to get the order of dose potentially deposited in tissue throughout the laboratory geometry.

Chapter 5

Dose measurements

5.1 Radiation measurements

For verification purposes direct dose measurements were carried out within the scope of this project. These were carried out with instruments (cf. section 5.2) designed for area monitoring and measurement of dose deposited from primarily non-directional sources of radiation (such as decay processes). This means that in our case of particle acceleration the doses may not be accounted for properly. Therefore, these measurements could not be viewed as an accurate measure of dose.

Doses were measured at different locations in the laboratory using above equipment: centered at $10\,\mathrm{cm}$ below the beam origin at distance of $45\,\mathrm{cm}$ from the chamber wall radius, at 0°, 15°, 30°, and 45° sideways of the beam direction, see Figure 6.9 in the results section. More locations were used for dose collection, but this was shown to be unfeasable due to low doses collected below background radiation. These cases were then simulated as doses deposited at the same locations, in a water phantom in the form of a cube with side length $10\,\mathrm{cm}$.

5.2 Measurement Equipment

The measurement equipment used are:

1. **Thermo Scientific SmartION 2120**, for detection of β- and γ-radiation. The instrument houses a $450\,\mathrm{cm}^3$ ionization chamber vented to the environment, thus operating at atmospheric pressures. Charges induced by incoming particles are determined by a MOSFET operational amplifier based electrometer. A movable shield made of $550\,\mathrm{mg\,cm}^2$ plastic allows for two modes of operation:

   - with it closed it gives the ambient equivalent dose calibrated for a uniform photon field

- with it closed it gives the ambient equivalent dose calibrated for a uniform field of electrons

For the current measurements, the shield was left open in order to collect dose in terms of ambient dose equivalent accurate for β in the range 150 keV–2.5 MeV to within 15 %, at a resolution of 0.1 μSv. The response from particles at higher energies in short burts is unknown.

2. **Thermo Scientific FH 40 G**, collecting only γ-radiation. It houses a proportional counter tube for radiation detection. Collects the accumulated ambient equivalent dose with a resolution of 10 nSv. For a uniform photon field the error is below 20 % in the energy range 25 keV–3 MeV.

3. **Thermo Scientific EPD-N2** is a personal radiation monitor. It is designed for collection of neutron radiation in the range 0.025 eV – 15 MeV with errors below a factor of 2, at a resolution of 10 μSv. Two separate silicon detectors able to distinguish between thermal/intermediate and fast neutrons. The first detector is covered in a plastic layer and detects fast neutrons via recoil protons emitted from the plastic. The other detector is covered in a ^{6}LiF scintillating layer and detects slow and intermediate neutrons [35].

Chapter 6

Results

6.1 Simulation results

Here the results from the simulations are presented: First, as doses collected directly in water phantoms and second, as dose maps constructed from particle flux.

6.1.1 Dose in water phantoms

Doses were collected using the water phantom for three different cases: the expected worst case scenario right in the beam direction in front of the chamber. in the doorway leading to the outer room with the existing lead shield open and with it closed, cf. Figure 6.1. Results are given in Sv per pC of accelerated primary electrons in Figure 6.2:a–c.

In the beam direction, the simulated doses are shown to be dominated by electrons at significant levels (of e.g. $2\,\mu\mathrm{Sv/pC}$ at $100\,\mathrm{MeV}$). With the lead door open, doses there are still dominated by electrons but at a significantly lower level of about $5\,\mathrm{pSv/pC}$ at $100\,\mathrm{MeV}$, a factor 10^6 lower than in the beam. With the lead screen closed, dose from neutrons (at around $0.2\,\mathrm{pSv/pC}$) dominate as electrons are effectively shielded.

6.1.2 Map of doses from particle flux

Figures 6.3–6.5, show maps over the dose deposited for electrons, gammas and neutrons, respectively, for the electron acceleration room. Doses are given per $1\,\mathrm{pC}$ of accelerated electrons and for an electron beam energy of $100\,\mathrm{MeV}$, $500\,\mathrm{MeV}$ and $1\,\mathrm{GeV}$.

A sliding lead screen with a thickness of $13\,\mathrm{cm}$ is located on the inside of the doorway leading to the outer room. Simulations show both cases: with lead screen open (left column) and closed (right column).

The dose distribution from electrons and gamma are shown follow similar behavior, being highly focused in the beam direction and becoming more

and more focused towards higher particle energies.

The dose distribution from neutrons are shown to be highly non-directional. Towards higher energies, the general distribution is not changed significantly, instead increasing the dose levels uniformly throughout the laboratory.
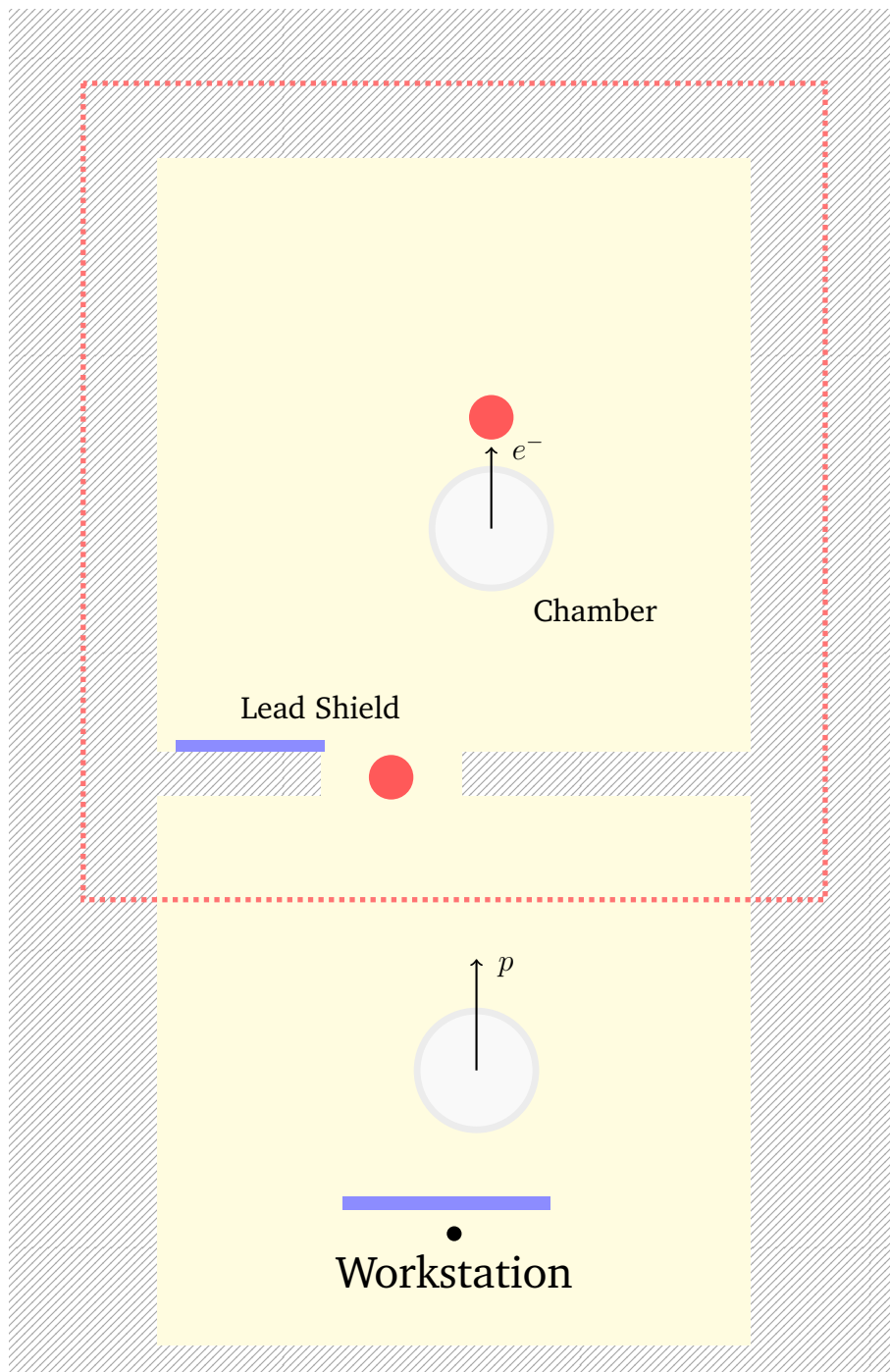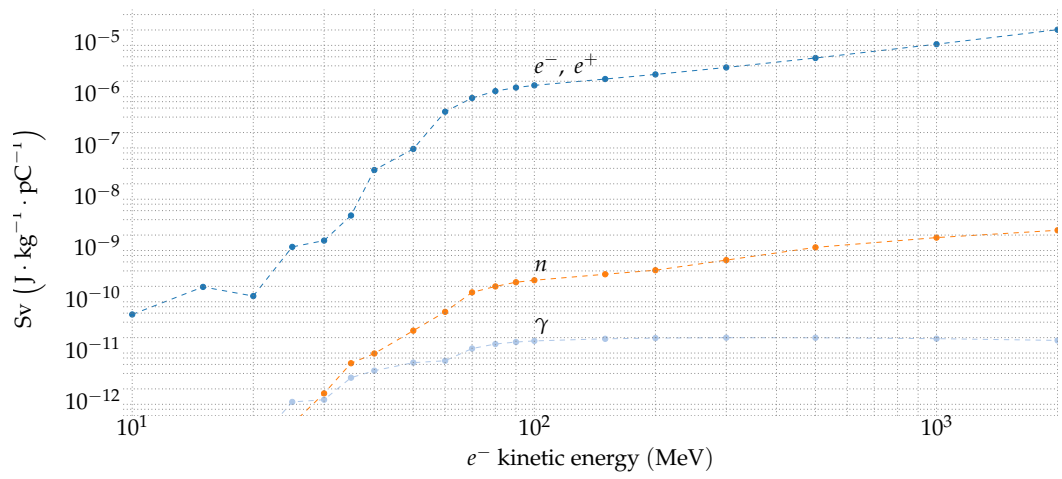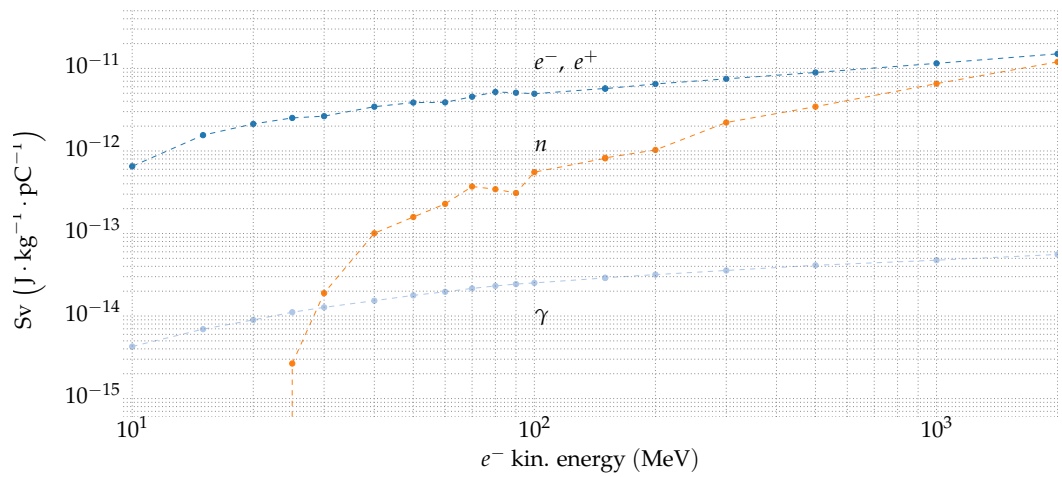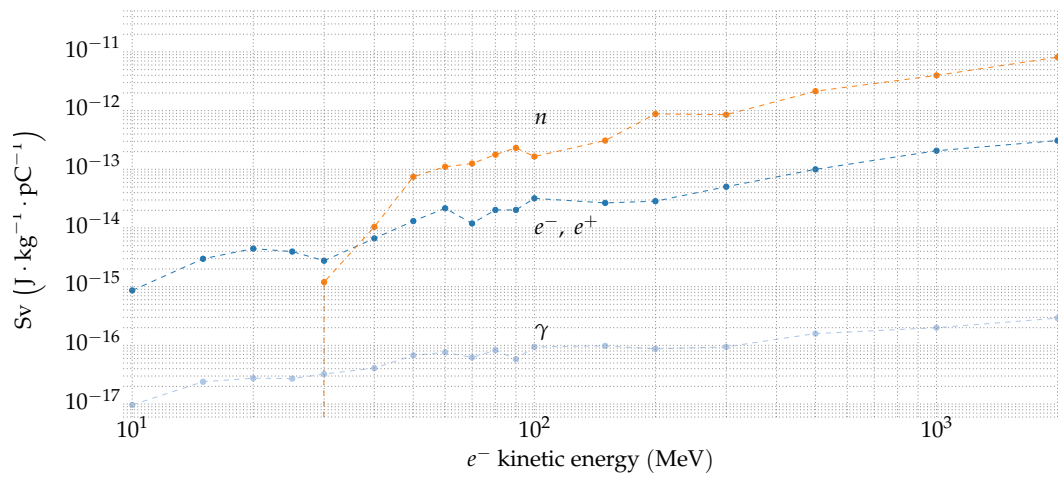
Figure 6.1: Layout sketch of the laboratory. Red filled circles show the simulated water phantom locations, in the beam direction and in the doorway.

(a) in beam

(b) at lead door (open)

(c) at lead door (closed)

Figure 6.2: Dose [Sv/pC] in water phantom for (a) the worst case scenario, directly in the beam outside the chamber; (b) in the doorway to the outer room, with lead shield open; (c) in the doorway to the outer room, with lead shield closed. Doses from absorbed electrons are shown to be dominant in the beam direction. At the position of the lead door, with it closed, doses from neutrons become dominant as electrons are effectively shielded.

(a) 100 MeV, lead screen open

(b) 100 MeV, lead screen closed

(c) 500 MeV, lead screen open

(d) 500 MeV, lead screen closed

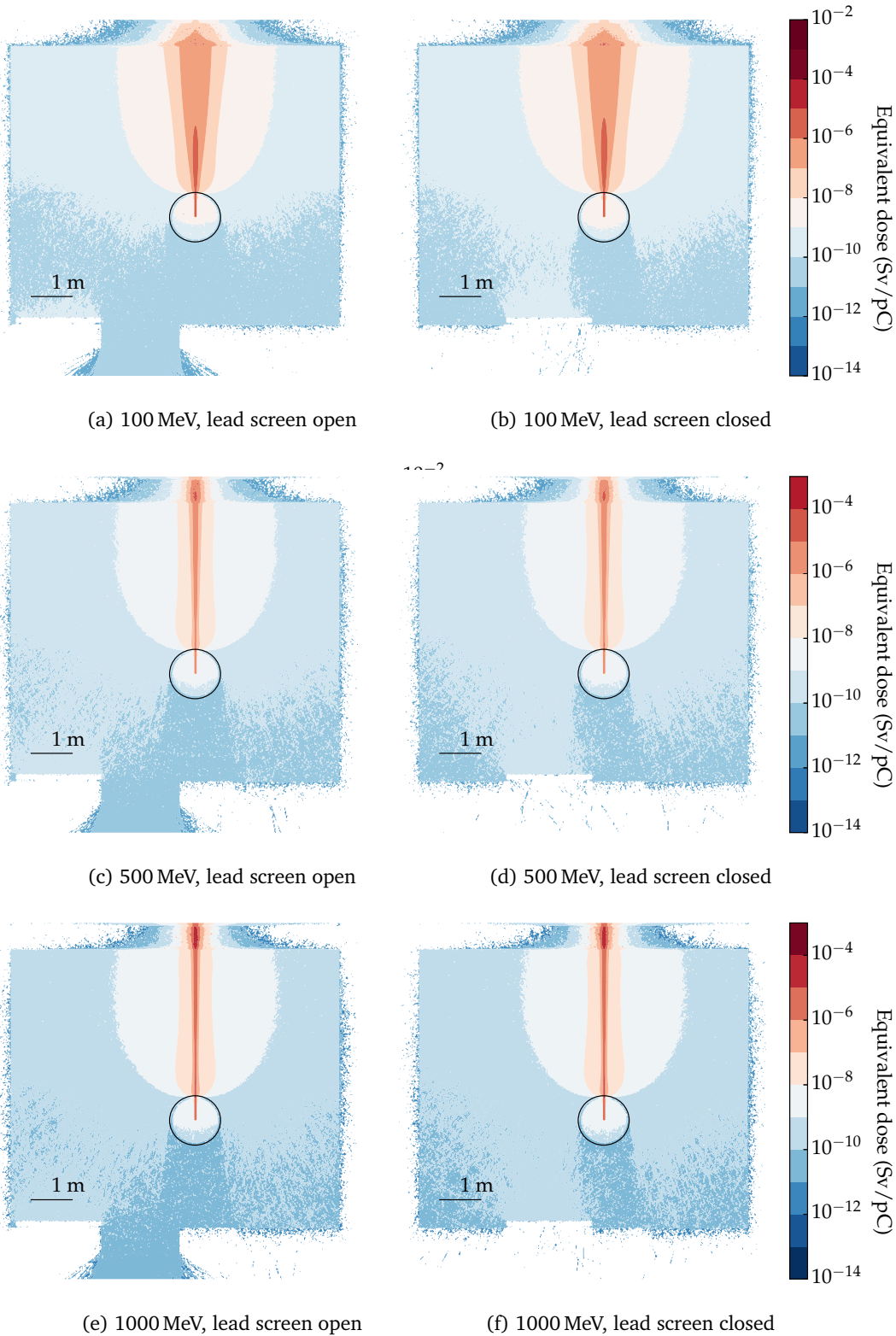(e) 1000 MeV, lead screen open

(f) 1000 MeV, lead screen closed

Figure 6.3: Electron doses [Sv/pC]. Lead door open (left column) and closed (right column). The distribution is shown to be highly directional, becoming more so towards higher energies. Doses quickly drop off going towards larger angles from the beam. The lead door effectively blocks out most radiation.

47

(a) 100 MeV, lead screen open   (b) 100 MeV, lead screen closed

(c) 500 MeV, lead screen open   (d) 500 MeV, lead screen closed

(e) 1000 MeV, lead screen open   (f) 1000 MeV, lead screen closed
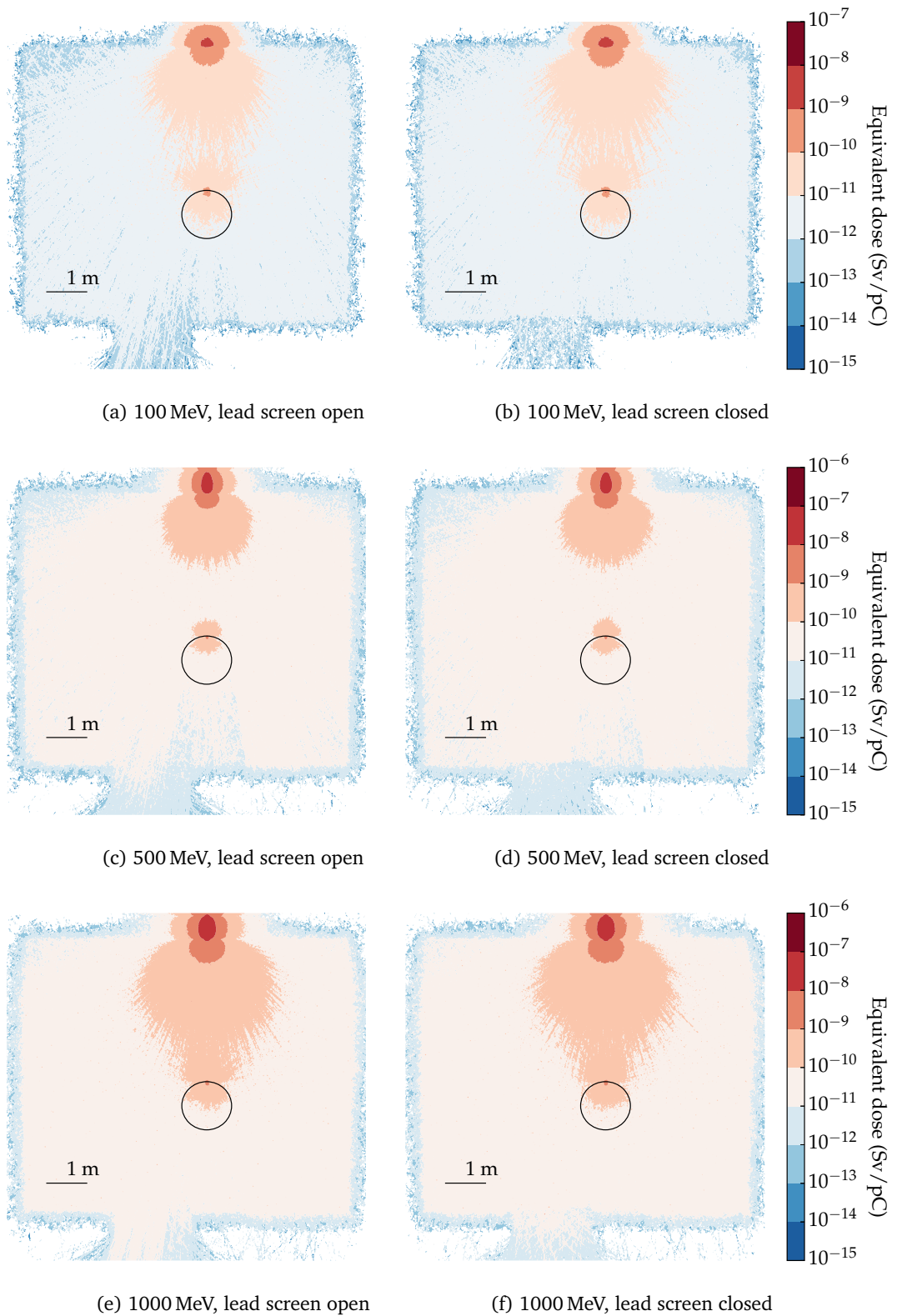
Figure 6.4: Neutron doses [Sv/pC]. Lead door open (left column) and closed (right column). Neutrons dose are distributed uniformly throughout the room. Going towards higher energies has the effect of raising the general dose levels in laboratory without changing the distribution very much. The lead door does not have a significant impact on the radiation levels.

(a) 100 MeV, lead screen open

(b) 100 MeV, lead screen closed

(c) 500 MeV, lead screen open

(d) 500 MeV, lead screen closed

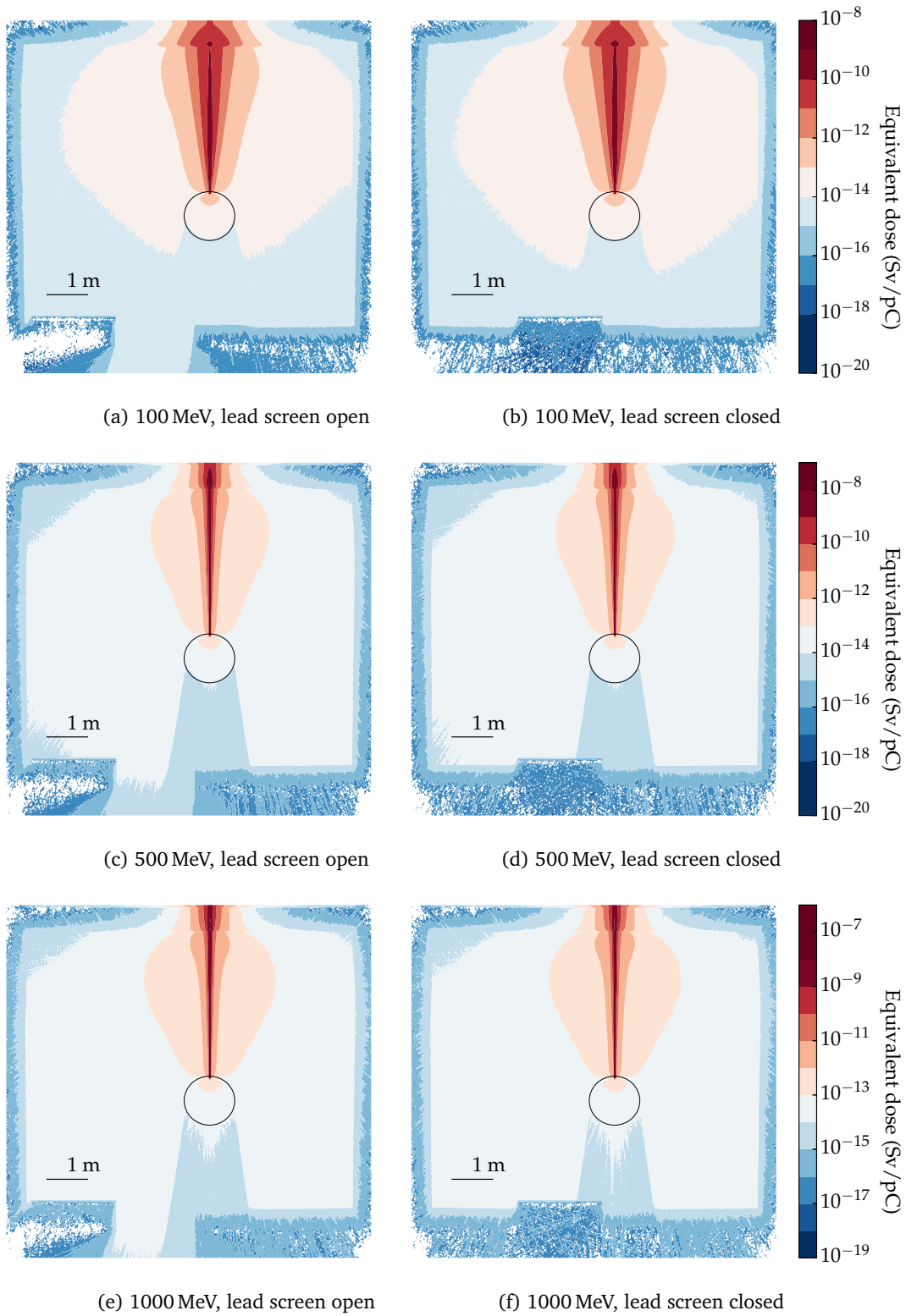(e) 1000 MeV, lead screen open

(f) 1000 MeV, lead screen closed

Figure 6.5: Gamma doses [Sv/pC]. Lead door open (left column) and closed (right column). Lead door open (left column) and closed (right column). As for electrons, the distribution is highly directional, becoming more focused in the beam direction at higher energies. Doses quickly drop off going towards larger angles from the beam. The lead door effectively blocks out most radiation.

6.1.3 Yearly charge limit

From the water phantom dose data and the yearly maximum dose limit of 20 mSv, a yearly maximum charge limit [pC] is determined, cf. figure 6.6.

Highest doses are generated for electrons accelerated to 2 GeV. Assuming electrons being produced in consistant high charge bunches of 200 pC it would require 10^7 shots to reach the dose limit of 20 mSv in a year. For a more reasonable assumption of 100 MeV electron in 100 pC bunches it would instead require 10^9 shots to reach the limit. This should be compared with the current situation where to date no more than 50,000 shots have been fired in a single year.

In the beam direction the potential risk is significantly higher, with only 10^2 shots at 100 MeV in 100 pC bunches needed to reach limit.
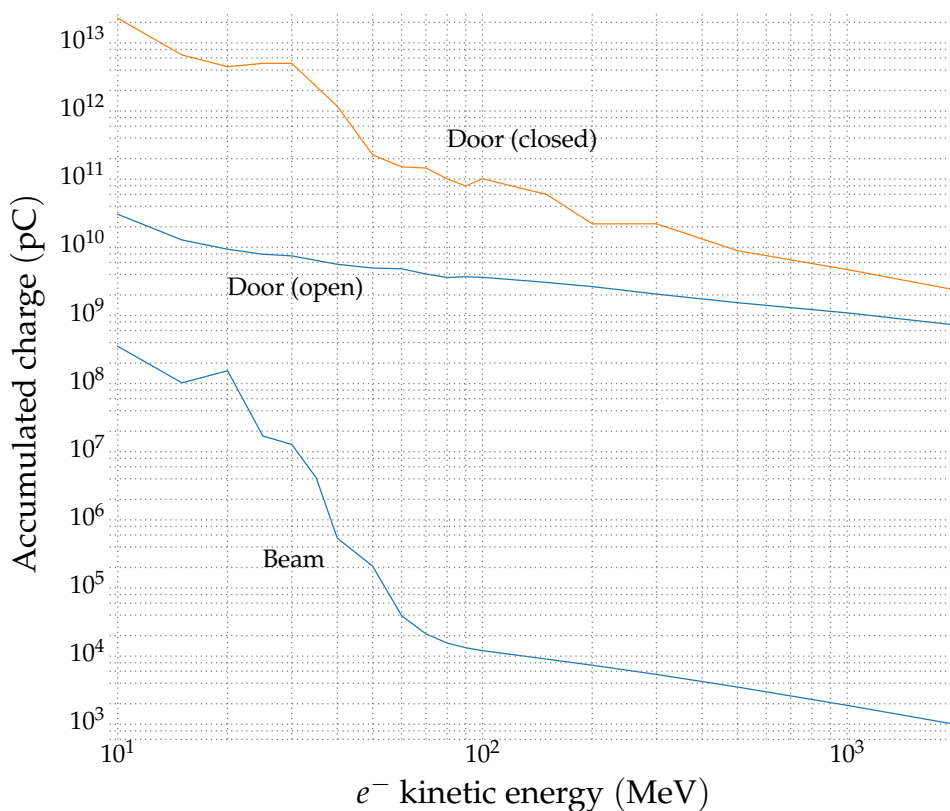

Figure 6.6: The accumulated electron beam charges needed to reach the yearly dose limit of 20 mSv. The orange line shows the case for when the lead door is closed.
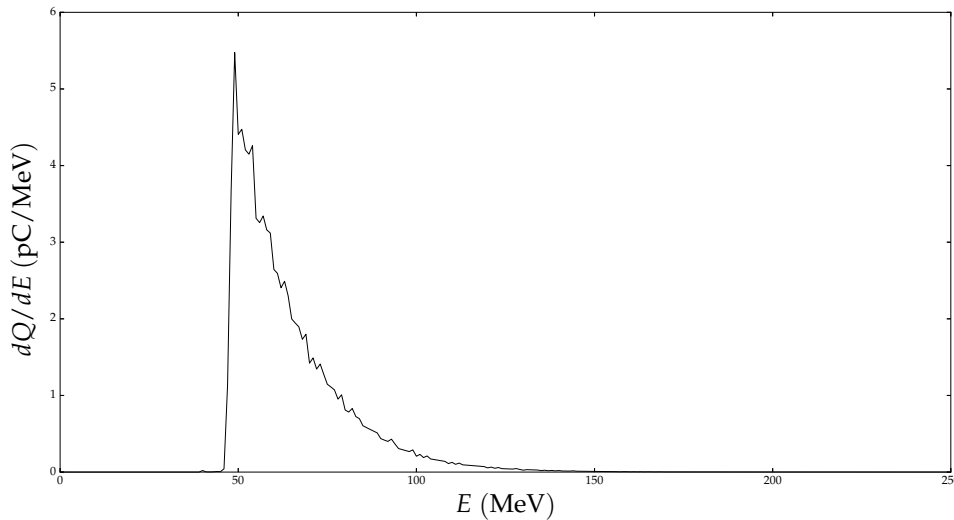
Figure 6.7: Spectrum of mean charge for the electron beams generated during a day of measurement. Due to the geometry of the electron spectrometer no reliable information of the charge content at energies below about 45 MeV was given..

6.2 Measurement results

Results from measurements and the corresponding simulations are shown in Figures 6.8:a–d. Here, the beam energy for a single shot was calculated based on the mean energy in the charge distribution of the electron for the few shots needed to get a significant signal where possible. The total charge for a given shot was determined by integration of each spectrum. Figure 6.7 shows the collection of charge distributions with a lower cutoff at around 45 MeV due to spectrometer design. The loss of information in the low energy part of the spectrum leads to higher energy and lower charge than the actual values. This means that the actual data points in figures 6.8:a–d should be shifted towards lower energy and lower dose per charge.

Error bars were calculated from the given maximum error in the measurement specifications together with the minimum and maximum in measured background radiation collected at the beginning and end of data collection. Since the energy range in generated particles exceed the range of operation for all three measurement devices, the error can be expected to be significantly larger to an undetermined degree.

6.2.1 Electron measurements

Electron doses show agreement with the simulated data in the forward direction (cf. 6.8:a). Increasing the detection angle, the measured data

deviates more from the simulations, where at 45 degrees the measured data show doses of about 4–6 times the simulated data.

6.2.2 Gamma measurements

Gamma doses were detected at such low levels that only in the forwards direction (Figure 6.8:a) it was possible to distinguish the experimental signal from the background radiation of 80–130 nSv·h^{-1}. The data points are grouped around 75 MeV and show doses around 5×10^{-11} Sv/pC, showing some agreement with the simulated dose of 2×10^{-11} Sv/pC.

6.2.3 Neutron measurements

Signals from neutrons were successfully detected only in the beam direction (0º). After 410 shots with an accumulated charge of 3740 pC and at an average energy of 64.1 MeV, a signal equivalent to 1 μSv was detected. This would give a neutron dose in the forwards beam direction of 2.7×10^{-10} Sv/pC but without any statistical certainty.

At 180º relative to the beam direction (cf. Fig. 6.9), no neutron signals were detected after 510 shots with an accumulated charge of 4530 pC and at an average energy of 64.7 MeV which at a resolution of 1 μSv gives an upper indicated limit of 2.2×10^{-10} Sv/pC.

Although these measurements cannot say much about the actual situation, they make it more plausible that neutron doses will lie below these levels at the measured energy.
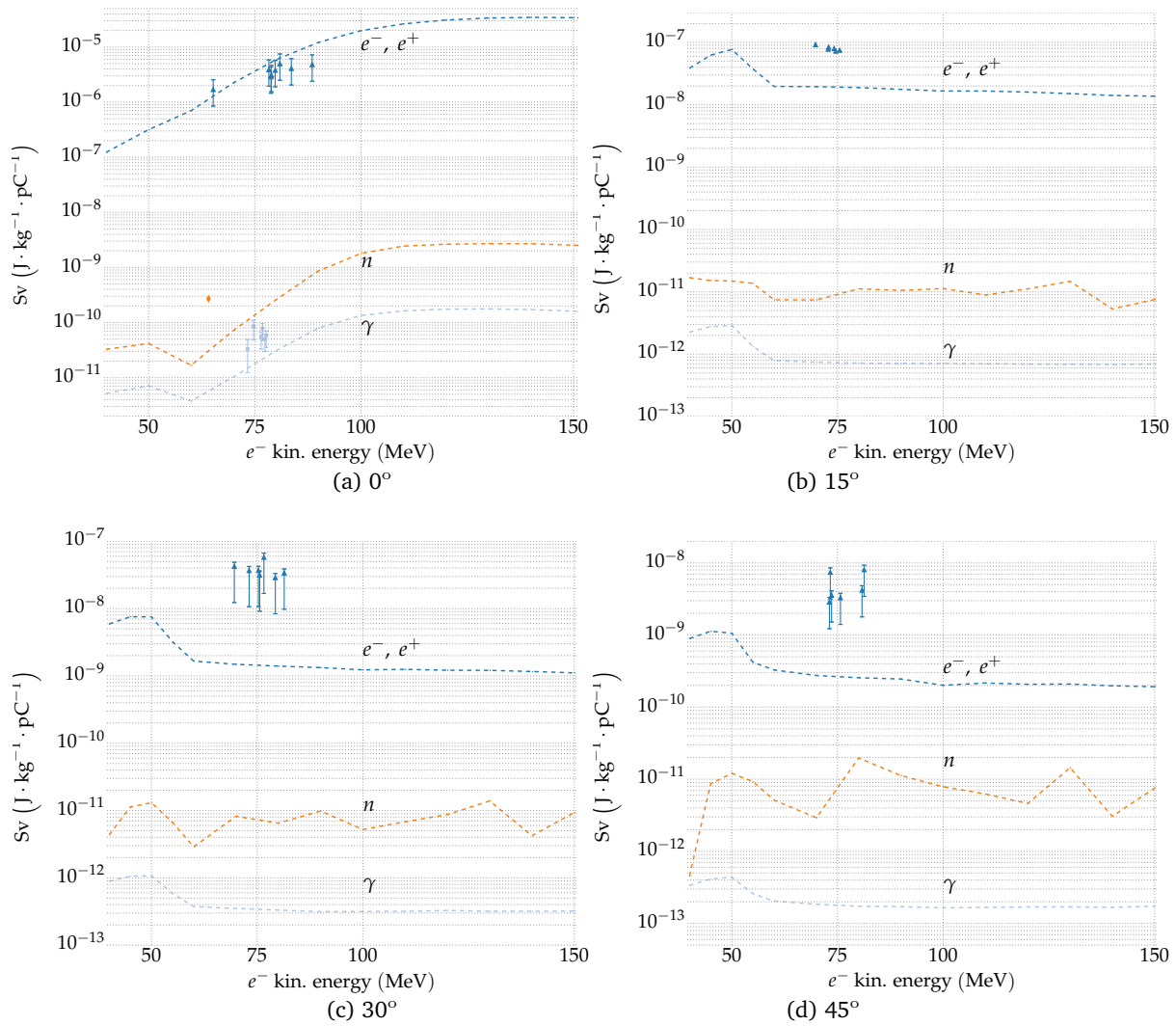
Figure 6.8: Dose data from simulations (dashed lines) and measurements (markers) at 0, 15, 30 and 45 degrees off beam direction, at a distance of 45 cm from the outer chamber wall radius, cf. Fig. 6.9. Matching colors for simulations and measurements indicate the particle type.
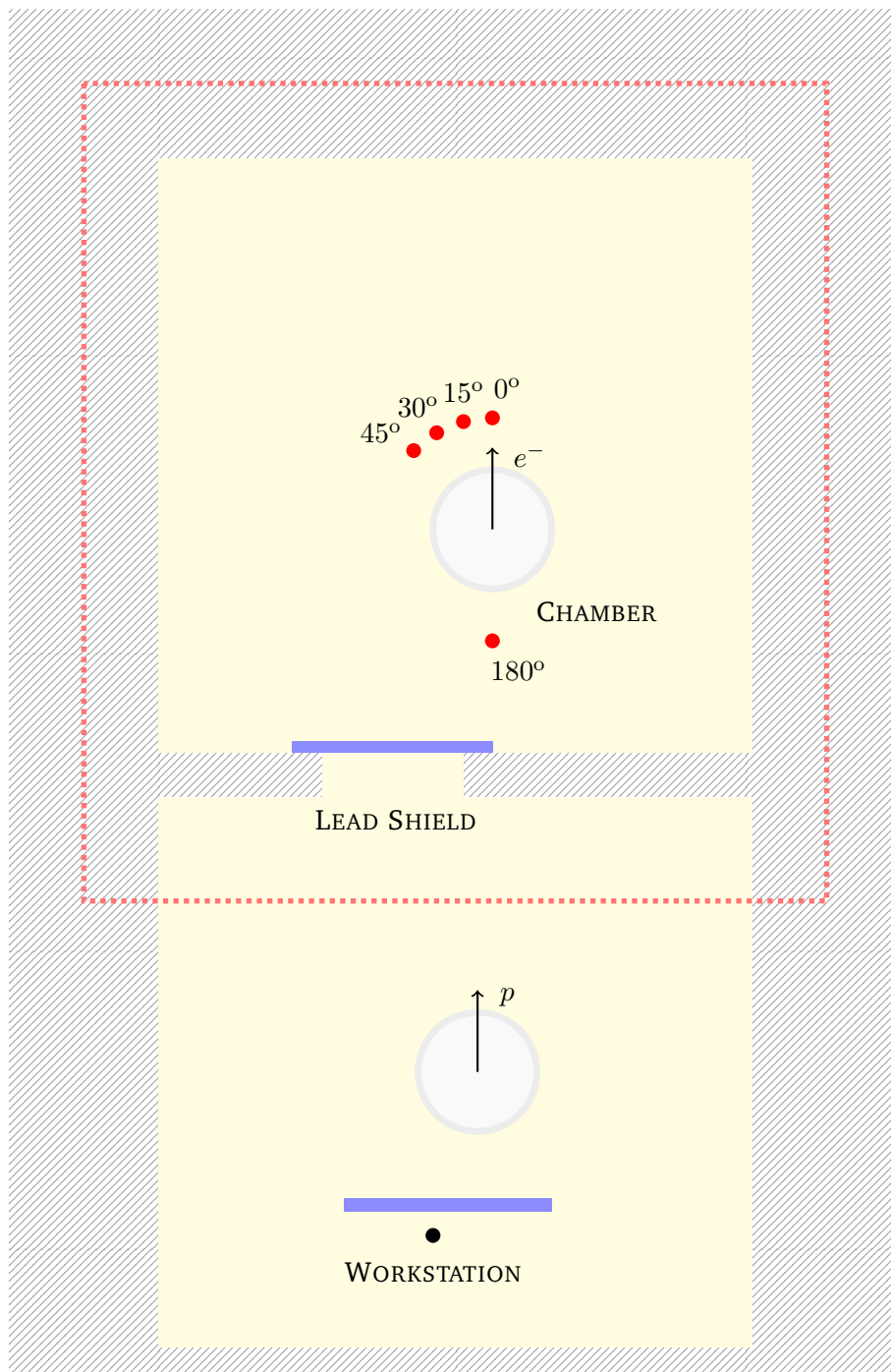
Figure 6.9: Layout sketch of the laboratory. Labeled red dots indicate measurement locations.

Chapter 7

Conclusions

This work was conducted as part in ensuring a safe working environment for the researchers of the laser-plasma acceleration of electrons at the Lund high-power laser facility, located at the Atomic Physics division of Lund University.

From the results of simulations conducted within this project, we have found the expected radiation dose levels to be well within acceptable limits for the current operation and for the foreseeable future. As long as the proper safety measures are taken, even for electron beams at $2\,\text{GeV}$ produced at the current repetition rate ($0.1\,\text{sec}^{-1}$), in excess of 10^7 pulses, in $200\,\text{pC}$ bunches are required to reach the yearly limit directly outside of the lead shield. This is far beyond the current operation since, to date, no single year has there been over 50,000 shots fired.

A natural continuation of this work would be to extend the simulations to also include the experiments involving the acceleration of protons, where significantly lower doses are expected.

The current work could be improved by construction of more complete simulations of the laboratory including most of its equipment—probably a project heavy in CAD construction of the geometry. It would then be advised to take use of the various biasing techniques available in order to reduce the computation times of similar simulations. Also more accurate direct dose measurements could be taken by using equipment designed for high particle energies in short bursts.

Bibliography

[1] S. Agostinelli et al. "GEANT4 – a simulation toolkit". In: *Nucl. Instrum. Meth.* A506 (2003) (cit. on pp. 6, 30).

[2] J. Allison et al. "Geant4 developments and applications". In: *IEEE Transactions on Nuclear Science* 53.1 (2006), pp. 270–278 (cit. on pp. 6, 30).

[3] M. Hansson. "Controlled Trapping in Laser Wakefield Accelerators". PhD thesis. Lund University, 2016 (cit. on pp. 8, 13–15).

[4] O. Lundh. "Laser-driven beams of fast ions, relativistic electrons and coherent x-ray photons". PhD thesis. Lund University, 2008 (cit. on p. 8).

[5] Thomas Katsouleas. "Accelerator physics: Electrons hang ten on laser wake". In: *Nature* 431.7008 (2004), pp. 515–516 (cit. on p. 12).

[6] Brice Quesnel and Patrick Mora. "Theory and simulation of the interaction of ultraintense laser pulses with electrons in vacuum". In: *Physical Review E* 58.3 (1998), p. 3719 (cit. on p. 13).

[7] P Sprangle, E Esarey, and A Ting. "Nonlinear theory of intense laser-plasma interactions". In: *Physical review letters* 64.17 (1990), p. 2011 (cit. on p. 13).

[8] Frank H. Attix. *Introduction to Radiological Physics and Radiation Dosimetry*. A Wiley-Interscience publication. Wiley, 1986 (cit. on pp. 19, 20, 28).

[9] S. Roesler, M. Silari, R. H. Thomas, and H. Schönbacher. "Radiation Effects and Protection". In: *Handbook of Accelerator Physics and Engineering*. Ed. by A. Wu Chao and M. Tigner. World Scientific, 2011. Chap. 8, pp. 647–702 (cit. on pp. 20, 21, 23, 26, 29).

[10] *1990 Recommendations of the International Commission on Radiological Protection*. ICRP Publication 60. Ann. ICRP 21 (1-3), 1990 (cit. on pp. 21–23, 25, 39).

[11] *2007 Recommendations of the International Commission on Radiological Protection*. ICRP Publication 103. Ann. ICRP 37 (2-4), 2007 (cit. on pp. 21–23, 26).

[12] *Radiation weighting factors*. https://www.euronuclear.org/info/encyclopedia/r/radiation-weight-factor.htm. European Nuclear Society (ENS). Accessed: 10 May 2016 (cit. on p. 22).

[13] *Directive 96/29/Euratom – ionizing radiation*. https://osha.europa.eu/sv/legislation/directives/73. 13 May 1996 (cit. on p. 22).

[14] *Directive 2013/59/Euratom – protection against ionising radiation*. https://osha.europa.eu/sv/legislation/directives/7. 5 December 2013 (cit. on p. 22).

[15] K. S. Krane. *Introductory Nuclear Physics*. Wiley, 1987 (cit. on p. 24).

[16] *ESTAR: stopping-power and range tables for electrons*. http://physics.nist.gov/PhysRefData/Star/Text/ESTAR.html. accessed: 2016-05-13 (cit. on p. 24).

[17] *Principles of Radiation Interactions*. http://ocw.mit.edu/courses/nuclear-engineering/22-55j-principles-of-radiation-interactions-fall-2004/lecture-notes/dos_calculations.pdf. Lecture notes (2004). Accessed: 2016-05-13 (cit. on p. 25).

[18] *X-Ray Mass Attenuation Coefficients*. http://physics.nist.gov/PhysRefData/XrayMassCoef/chap3.html. accessed: 2016-05-13 (cit. on p. 25).

[19] *X-Ray Mass Attenuation Coefficient Data*. http://www.nist.gov/pml/data/xraycoef/index.cfm. accessed: 2016-05-13 (cit. on p. 25).

[20] A.V. Sannikov and E.N. Savitskaya. "Ambient Dose Equivalent Conversion Factors for High Energy Neutrons Based on the ICRP 60 Recommendations". In: *Radiation Protection Dosimetry* 70.1-4 (1997), pp. 383–386 (cit. on p. 25).

[21] G. Leuthold, V. Mares, and H. Schraube. "Calculation of the Neutron Ambient Dose Equivalent on the Basis of the ICRP Revised Quality Factors". In: *Radiation Protection Dosimetry* 40.2 (1992), pp. 77–84 (cit. on p. 25).

[22] J. Strandman. *SSMFS 2008:51 Strålskyddsmyndighetens föreskrifter om grundläggande bestämmelser för skydd av arbetstagare och allmänhet vid verksamhet med joniserande strålning*. ISSN 2000-0987. Swedish Radiation Safety Authority, 2008 (cit. on p. 26).

[23] *Strålskyddets principer inklusive hygieniska gränsvärden*. http://www.stralskydd.med.lu.se/ss_grv.htm. accessed: 2016-05-16 (cit. on p. 26).

[24] W. P. Swanson. *Radiological Safety Aspects of the Operation of Electron Linear Accelerators*. IAEA, 1979 (cit. on p. 26).

[25] B. R. Martin and G. Shaw. *Particle Physics*. 3rd ed. Wiley, 2008 (cit. on p. 27).

[26] F. Ferroni, L.A. Gizzi, R. Faccini, and Società italiana di fisica. *Laserplasma Acceleration: Proceedings of the International School of Physics*. International School of Physics Enrico Fermi. IOS Press, 2012 (cit. on pp. 27–29).

[27] Vaclav Vylet and James C Liu. "Radiation protection at high energy electron accelerators". In: *Radiation Protection Dosimetry* 96.4 (2001), pp. 333–343 (cit. on pp. 28, 29).

[28] Pierre L'ecuyer. "Efficient and portable combined random number generators". In: *Communications of the ACM* 31.6 (1988), pp. 742–751 (cit. on p. 30).

[29] Frederick James. "A review of pseudorandom number generators". In: *Computer Physics Communications* 60.3 (1990), pp. 329–344 (cit. on p. 30).

[30] *Geant4 Material Database*. geant4.web.cern.ch/geant4/workAreaUserDocKA/Backup/Docbook_UsersGuides_beta/ForApplicationDeveloper/html/apas08.html. accessed: 2016-05-10 (cit. on p. 32).

[31] C. M. Poole. *CADMesh – a CAD file interface for GEANT4*. Git repository: https://github.com/christopherpoole/CADMesh. accessed: 2016-05-23 (cit. on pp. 32, 35).

[32] *Geant4 10.2 Application Developer Guide*. http://geant4.web.cern.ch/geant4/UserDocumentation/UsersGuides/ForApplicationDeveloper/html/index.html. Published: 4 Dec 2015 (cit. on pp. 33, 34, 38, 39).

[33] *Geant4 Reference Physics Lists*. http://geant4.cern.ch/support/proc_mod_catalog/physics_lists/referencePL.shtml. accessed: 2016-05-10 (cit. on pp. 33, 38, 60).

[34] C. M. Poole, I. Cornelius, J. V. Trapp, and C. M. Langton. "A CAD Interface for GEANT4". In: *Australasian Physical & Engineering Science in Medicine* (2012) (cit. on p. 35).

[35] M Luszik-Bhadra, J Coleman, D Schlegel, and A Zimbal. "Active neutron/photon personal dosemeters". In: Preprint of a paper presented at the European IRPA Congress. 2002 (cit. on p. 42).

[36] *Geant4 10.2 Physics Reference Manual*. http://geant4.web.cern.ch/geant4/UserDocumentation/UsersGuides/PhysicsReferenceManual/fo/PhysicsReferenceManual.pdf. Published: 2015-12-04 (cit. on pp. 60–62).

[37]   National Nuclear Data Center. *Evaluated Nuclear Data File (ENDF/B)*. http://www.nndc.bnl.gov/exfor/endf00.jsp (cit. on p. 60).

[38]   H. W. Koch and J. W. Motz. "Bremsstrahlung Cross-Section Formulas and Related Data". In: *Rev. Mod. Phys.* 31 (4 1959), pp. 920–955 (cit. on p. 61).

[39]   JMC Brown, MR Dimmock, JE Gillam, and DM Paganin. "A low energy bound atomic electron Compton scattering model for Geant4". In: *Nuclear Instruments and Methods in Physics Research Section B: Beam Interactions with Materials and Atoms* 338 (2014), pp. 77–88 (cit. on p. 62).

[40]   MJ Berger and JH Hubbell. *XCOM, Photon cross sections on a personal computer. Report No. NBSIR87–3597. Gaithersburg, MD: NIST; 1987* (cit. on p. 62).

[41]   L. Kissel D. Cullen J. H. Hubbell. "EPDL97: the Evaluated Photon Data Library, 97 version". In: *UCRL–50400* 6.Rev. 5 (1997) (cit. on p. 62).

Appendix A

GEANT4 physics processes

Abbreviations used in the relevant physics list are listed below:

- `QGSP` *(quark-gluon string precompound)*. The Quark-Gluon String Precompound model is built from several component models which handle various parts of a high energy collision of energies above (12 GeV). The quark-gluon string (QGS) part handles the formation of strings in the initial collision of a hadron with a nucleon in the nucleus. String fragmentation into hadrons is handled by the Quark-Gluon String fragmentation model. The precompound part handles the de-excitation of the remnant nucleus. The current project concerns too low energies for this model to become relevant.

- `BERT` *(Bertini Cascade)*. Uses the Bertini model [36] of inelastic scattering of hadrons colliding with protons and neutrons inside the target nucleus. Applicable for energies of approximately 0–10 GeV.

- `HP` *(High Precision neutron model)*. Model using experimental data [37] for neutron absorption to track neutron from kinetic energies of $E_n < 20$ MeV down to thermal energies [33].

A.1 Reference physics list implemented

The implemented physics process is based on the pre-built physics list `QGSP_BERT_HP`. It is designed for general radiation shielding and and neutron interaction at all energies.

For neutrons at energies below 20 MeV, interaction cross-sections for elastic scattering, inelastic scattering, neutron capture and fission are taken from experimental data (`G4NDL-4.5`) in the ENDF/B-VII library [37]. This is indicated by the HP (high precision) in the name, e.g. `NeutronHPElastic`.

A.1.1 Package for electromagnetic processes

The standard electromagnetic package of `QGSP_BERT_HP` has been replaced
with `G4EmStandard_option4` providing a more accurate model for the scat-
tering angles in a bremsstrahlung cascade.
For reference, a list over the processes used in `G4EmStandard_option4`
are included. For more information cf. the Geant Physics Reference Man-
ual [36].

A.1.2 Bremsstrahlung

This handles energy losses of electrons and positrons due to radiation of
photons. In this model, cross sections take the form

$$\frac{d\sigma}{dk} = \frac{d\sigma_n}{dk} + Z\frac{d\sigma_e}{dk}, \tag{A.1}$$

and are made of of the two different cross-sections for bremsstrahlung,
from scattering off of the electric field of the nucleus, $d\sigma_n/dk$, or the field
of the atomic electrons, $d\sigma_e/dk$, cf. section 3.5.1.
Values for cross-sections $d\sigma_n/dk$ and $d\sigma_e/dk$ are dependent on both the
energy of incident particle and on the energy k of the produced photon.
Included in `G4EmStandard_option4` a more accurate model of the angular
distribution of exit photons compared to the standard `G4EmStandard`. This
angular distribution is handled by the class `G4Generator2BS` which relies
on interpolation of data given by Koch and Motz [38].

Coulomb scattering

`G4eCoulombScattering` handles the elastic scattering in charged particle
interactions. For e^+/e^+ in the range 100 MeV–10 TeV; for p in the range
0 MeV–10 TeV.

Multiple scattering

Concerns the elastic scattering of electrons and other charged particles.
Compared to eCoulombScattering it has a simpler calculation scheme for
the elastic scattering of electrons at low energies, which is needed for ac-
ceptable CPU performance.
$e-$, $e+$: `G4UrbanMsc` at 0–100 MeV, `G4WentzelVIUni` at 100 MeV–10 TeV.
p, generic ions: `G4WentzelVIUni` at 0 MeV–10 TeV

Compton scattering

Compton scattering is the inelastic scattering of a photon by an electron.
Here handled by two separate models based on gamma energy: by

`G4LowEPComptonModel` up to 20 MeV, and `G4KleinNishinaModel` from 20 MeV and up.

`G4LowEPComptonModel` extends the operation of `G4LivermoreComptonModel` by use of a two-body fully relativistic three-dimensional scattering framework for energy and momentum conservation in the relativistic impulse approximation. Here, energy and scattering angles for both the scattered photon and ejected Compton electron is drawn from first principles [39].

Pair production

Also known as γ-conversion. Is handled here by `G4PenelopeGammaConversion` and cross sections [36] are determined from NIST data [40]; energy E interpolated from data between energies E_1 and E_2 (with cross sections σ_1 and σ_2 respectively).

Photoelectric effect

The photoelectric process concerns incident γ and is modeled by the class `G4LivermorePhotoElectricModel` which is based on EPDL97 cross sections [41].

The incident photon is absorbed and an electron is emitted. The sub-shell from where the electron is emitted is sampled based on the relative cross-section of all sub-shells at the given energy.